JEM Journal of Experimental Medicine

ARTICLE

Sensing of metabolic signals via GPR183 promotes occupation of lung macrophage niches by monocytes

Laura Bub[1*], Elza Evren[1*], Stijn Verwaerde[2,3*], Cecilia Ruscitti[4,5**], Domien Vanneste[4,5**], Pia Ghosh[6,7,8], Yu Gao[1], Natalie Sleiers[1], Rong Deng[1], Marta López Montes[1], Kelsey Howley[9], Raphaël La Rocca[4,5], Annika Niehrs[1], Vassilis Glaros[10,11], Maria Reina-Campos[12], Barbro Dahlen[6], Anna Smed-Sörensen[10], Harald Lund[12], Taras Kreslavsky[10], Niklas K. Björkström[1], Andrea Reboldi[9], Apostolos Bossios[6,7,8], Thomas Marichal[4,5,13***], Bart N. Lambrecht[2,3***], and Tim Willinger[1***]

Monocytes populate tissues when local niches are depleted of tissue-resident macrophages, yet the tissue-derived signals controlling monocyte-to-macrophage differentiation are largely undefined. Here, we discovered that the oxysterol receptor GPR183 positions monocytes to sense niche signals that induce lung macrophage differentiation. We found that interstitial macrophages that continuously turn over express the oxysterol receptor GPR183, whereas alveolar macrophages that derive from embryonic progenitors and slowly turn over did not. Models of conditional tissue-resident macrophage depletion showed that newcomer monocyte-derived macrophages expressed GPR183 along their differentiation trajectory. Recruited GPR183$^+$ monocytes interacted with fibroblasts and lack of GPR183 caused defective lung macrophage differentiation. Single-cell RNA analysis over time identified lung fibroblasts as the source of the GPR183 ligand 7α,25-dihydroxycholesterol in the empty niche. Our findings identify oxysterols as instructive signals for tissue-resident macrophage development from monocytes.

Introduction

The lung is continuously exposed to the outside environment and therefore a common target of infection and inflammation. Macrophages are the most abundant immune cell type in the lungs and are strategically positioned in the interstitium and alveoli, where the gas exchange takes place (Aegerter et al., 2022; Bain and MacDonald, 2022; Evren et al., 2020; Kulikauskaite and Wack, 2020). Mouse studies have shown that tissue macrophages either derive from embryonic progenitors or from hematopoietic stem cell–derived monocytes. In steady state, tissue-resident mouse alveolar macrophages develop from fetal monocytes, acquiring their typical identity under the influence of the instructive cytokines GM-CSF (Gschwend et al., 2021; Guilliams et al., 2013; Shibata et al., 2001) and TGFβ (Yu et al., 2017) and transcription factors, such as PPARγ (Schneider et al., 2014), BHLHE40/BHLHE41 (Rauschmeier et al., 2019), and EGR2 (McCowan et al., 2021). In homeostatic conditions, tissue-resident macrophages are maintained in the alveolar niche mostly by local self-renewal independent of input from bone marrow monocytes (Guilliams et al., 2013; Hashimoto et al., 2013; Soucie et al., 2016; Subramanian et al., 2022; Yona et al., 2013). Tracking macrophage origin in humans undergoing lung transplantation suggests that human alveolar macrophages are replenished to a greater degree by blood monocytes than mouse alveolar macrophages (Byrne et al., 2020). Macrophages also reside in the interstitial tissue space of the lung, with distinct subsets of interstitial macrophages differing in anatomical location, lifespan, replenishment, and function (Chakarov et al., 2019; Dick et al., 2022; Gibbings et al., 2017; Li et al., 2024; Schyns et al., 2019; Ural et al., 2020). Interstitial lung macrophages require the cytokines macrophage-CSF (M-CSF) and TGFβ as well as MAF transcription factors (Peng et al., 2025; Vanneste et al., 2023). Compared with their counterparts in the alveoli, interstitial lung macrophages are more dependent on bone marrow–derived monocytes in the steady state (Chakarov et al., 2019; Dick et al., 2022).

---

[1]Department of Medicine Huddinge, Center for Infectious Medicine, Karolinska Institutet, Karolinska University Hospital, Stockholm, Sweden; [2]Laboratory of Immunoregulation and Mucosal Immunology, VIB-UGent Center for Inflammation Research, Ghent, Belgium; [3]Department of Internal Medicine and Pediatrics, Ghent University, Ghent, Belgium; [4]Laboratory of Immunophysiology, GIGA Institute, University of Liège, Liège, Belgium; [5]Faculty of Veterinary Medicine, University of Liège, Liège, Belgium; [6]Department of Respiratory Medicine and Allergy, Karolinska University Hospital, Stockholm, Sweden; [7]Division for Lung and Airway Research, Institute of Environmental Medicine, Karolinska Institutet, Stockholm, Sweden; [8]Lung Laboratory, Center for Molecular Medicine, Karolinska University Hospital, Stockholm, Sweden; [9]Department of Pathology, Immunology, and Microbial Pathogenesis Program, University of Massachusetts Chan Medical School, Worcester, MA, USA; [10]Division of Immunology and Respiratory Medicine, Department of Medicine Solna, Karolinska Institutet, Karolinska University Hospital, Stockholm, Sweden; [11]Center for Molecular Medicine, Karolinska University Hospital, Stockholm, Sweden; [12]Department of Physiology and Pharmacology, Karolinska Institutet, Stockholm, Sweden; [13]Walloon Excellence in Life Sciences and Biotechnology (WELBIO) Department, WEL Research Institute, Wavre, Belgium.

*L. Bub, E. Evren, and S. Verwaerde contributed equally to this paper; **C. Ruscitti and D. Vanneste contributed equally to this paper; ***T. Marichal, B.N. Lambrecht, and T. Willinger share senior authorship. Correspondence to Tim Willinger: tim.willinger@ki.se; Bart N. Lambrecht: Bart.Lambrecht@UGent.be; Thomas Marichal: T.Marichal@uliege.be.

https://doi.org/10.1084/jem.20252667

Spontaneous replenishment of tissue-resident macrophages as well as perturbed organ homeostasis triggers the recruitment of monocytes from the circulation into tissues. In mice and humans, CCR2-dependent Ly6C^{hi} and CD14^{+} classical monocytes, respectively, can differentiate into monocyte-derived macrophages in the lung (Aegerter et al., 2022; Evren et al., 2021; Neehus et al., 2024; T'Jonck and Bain, 2023; Trzebanski et al., 2024) and other organs (Guilliams et al., 2018). An important driver of this differentiation is the state of the macrophage niche, made up of stromal cells like fibroblasts, endothelial cells, and epithelial cells, that together provide the signals that determine monocyte fate (Bonnardel et al., 2019; Guilliams et al., 2020). In steady-state conditions, and with minimal derangement of the niche, monocytes replacing tissue-resident macrophages as part of a normal replenishment process acquire a phenotype and function that is hardly distinguishable from the original tissue-resident macrophages that derive from embryonic progenitors (Gibbings et al., 2015; van de Laar et al., 2016). However, when organ homeostasis is perturbed, a monocyte differentiating in an inflammatory niche might become a pro-fibrotic or pro-inflammatory macrophage with functions that are distinct from steady-state tissue-resident macrophages in that niche (Iliakis et al., 2025; T'Jonck and Bain, 2023). In support of this scenario, tissue-resident lung macrophages are replaced by infiltrating blood monocytes in severe respiratory infections or in chronic inflammatory lung diseases like asthma and chronic obstructive pulmonary disease, where they can determine the outcome of lung injury on a spectrum from complete resolution after injury, over altered immune responsiveness to debilitating remodeling and fibrosis (Aegerter et al., 2020; Li et al., 2022a; Machiels et al., 2017; Mirchandani et al., 2022; Misharin et al., 2017; Ruscitti et al., 2024; Szabo et al., 2021; Theobald et al., 2024; Wendisch et al., 2021).

The molecular signals controlling the development and function of monocyte-derived macrophages in the lung niche in homeostasis and disease remain poorly understood. Furthermore, the local cues that guide monocytes to specific macrophage niches in the lung are largely undefined. G protein–coupled receptors (GPCRs) are an important receptor family that allows cells to respond to diverse signals from their surrounding tissue microenvironment. One such GPCR expressed in immune cells is GPR183 (also known as EBI2), a cell surface receptor for hydroxylated cholesterol metabolites, called oxysterols (Cyster et al., 2014; Dang and Reboldi, 2024). The GPR183 ligand 7α,25-dihydroxycholesterol is generated from cholesterol by the enzymes cholesterol 25-hydroxylase (CH25H) and 7α-hydroxylase (CYP7B1). The enzyme hydroxy-δ-5-steroid dehydrogenase, 3 β- and steroid δ-isomerase 7 (HSD3B7) degrades 7α,25-dihydroxycholesterol into bile acid precursors. Oxysterols recognized by GPR183 control the migration and positioning of immune cells within lymphoid (Baptista et al., 2019; Gatto et al., 2009, 2013; Li et al., 2016; Pereira et al., 2009; Yi and Cyster, 2013) and nonlymphoid organs (Bohrer et al., 2022; Emgård et al., 2018) as well as immune responses.

Here, using reporter and gene-deficient mice, we uncover GPR183 as a receptor for metabolic signals that determine monocyte localization within the lung and monocyte differentiation into macrophages after experimental niche depletion and lung injury. Macrophage development from monocytes required a non-hematopoietic source of GPR183 ligand with fibroblasts as the main producers of 7α,25-dihydroxycholesterol. GPR183 promoted the interaction of recruited monocytes with lung fibroblasts and their differentiation into alveolar and interstitial macrophages. Monocytes accumulating in the chronically inflamed airways of humans with bronchiectasis, a neglected but important lung disease, also expressed the oxysterol receptor GPR183. Our results provide a mechanism of how the sensing of cholesterol metabolites after macrophage depletion links niche signals to macrophage differentiation from monocytes.

Results

Anatomical niche impacts GPR183 expression by lung macrophages

We hypothesized that monocytes use GPR183 to sense metabolic signals in the lung. To explore this hypothesis, we first investigated the expression of GPR183 in lung monocytes and macrophages. Analysis of *Gpr183*$^{GFP/+}$ reporter mice demonstrated that Ly6C^{hi} and Ly6C^{lo} lung monocytes expressed *Gpr183* mRNA (Fig. 1 A and Fig. S1 A). Lung dendritic cells and eosinophils also expressed *Gpr183*-GFP, whereas neutrophils were largely GFP^{-} (Fig. 1 A). B lymphocytes highly expressed *Gpr183* mRNA, whereas CD4 and CD8 T cells showed lower expression (Fig. 1 B). *Gpr183* was required for monocyte migration toward 7α,25-dihydroxycholesterol *in vitro* (Fig. 1 C), consistent with functional GPR183 expression on the cell surface. These results identify the GPR183 ligand 7α,25-dihdroxycholesterol as a chemoattractant for monocytes. Like monocytes, both CD206^{+} and CD206^{-} interstitial lung macrophages transcribed *Gpr183* mRNA (Fig. 2, A and B; and Fig. S1 A). In contrast, *Gpr183* mRNA was not expressed by resident alveolar macrophages (Fig. 2 A and Fig. S1 A) that are derived from fetal monocytes (Guilliams et al., 2013; Schneider et al., 2014). The number of Ly6C^{hi} lung monocytes, interstitial lung macrophages, and alveolar macrophages was not different in *Gpr183*$^{+/+}$ and *Gpr183*$^{-/-}$ mice (Fig. 2 C). Therefore, GPR183 was not required for the homeostasis of resident macrophages in the steady-state lung.

We next asked whether alveolar macrophages derived from bone marrow monocytes expressed *Gpr183*. For this purpose, we generated bone marrow chimeras, where irradiated B6 recipient mice (CD45.1^{+}) were transplanted with bone marrow from *Gpr183*^{GFP} reporter mice (CD45.2^{+}) (Fig. 2 D). Whole-body irradiation leads to the replacement of resident lung macrophages (CD45.1^{+}) by macrophages derived from donor monocytes (CD45.2^{+}). Flow cytometry analysis revealed that CD45.2^{+} monocyte–derived lung macrophage populations, including transitional CD11c^{+}SiglecF^{mid} alveolar macrophages, expressed *Gpr183* at 3 wk after bone marrow transfer (Fig. 2 E and Fig. S1 B). In contrast, monocyte-derived alveolar macrophages with a mature CD11c^{+}SiglecF^{hi} surface phenotype expressed lower amounts of *Gpr183* mRNA (Fig. 2 E). Low *Gpr183* mRNA expression was maintained by CD45.2^{+} monocyte–derived alveolar macrophages at 5 wk after bone marrow reconstitution and eventually downregulated at 12 wk (Fig. 2 F). *Gpr183* downregulation was also observed *in vitro*

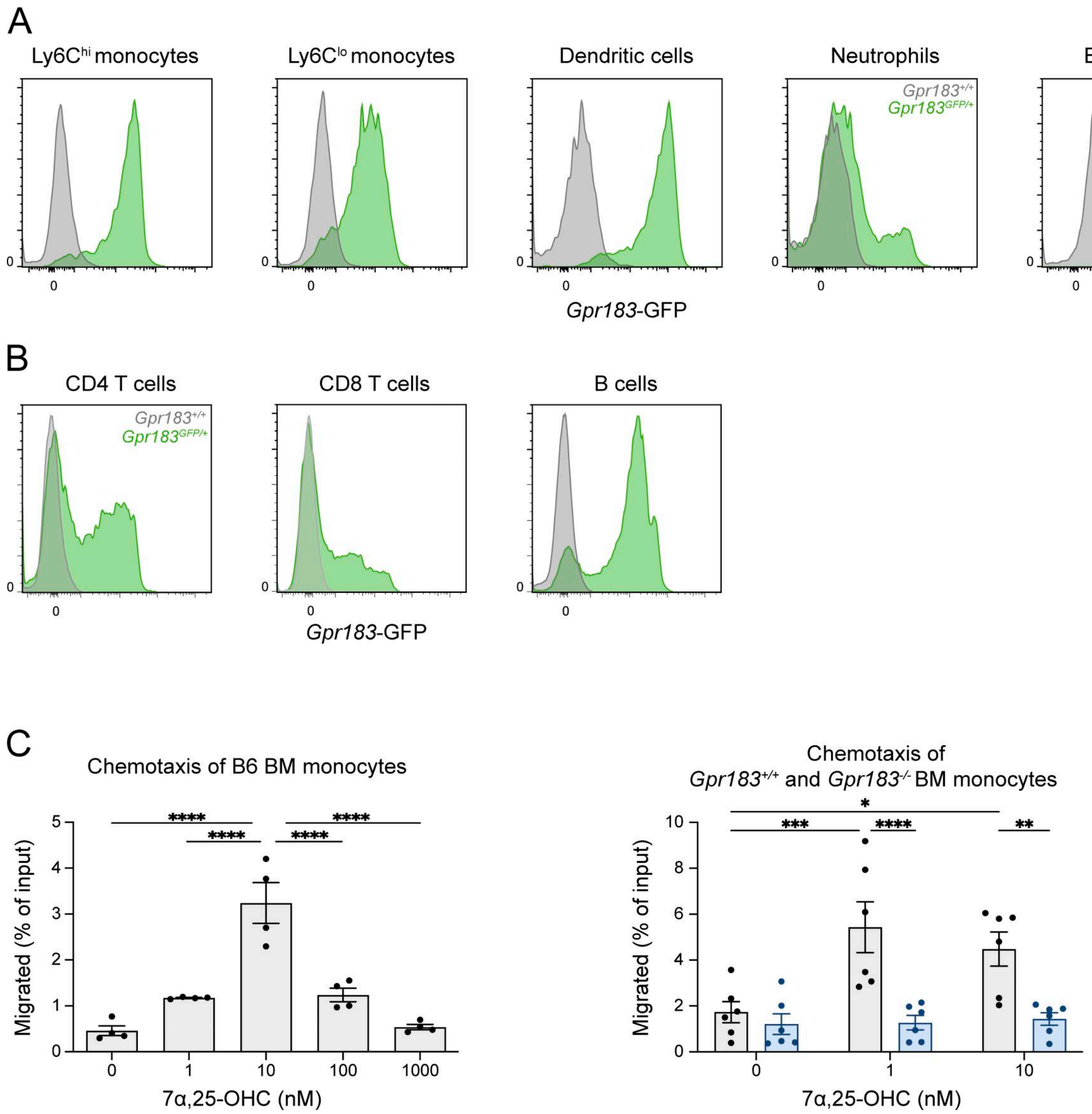

Figure 1. **Lung monocytes express GPR183 and migrate toward 7α,25-dihydroxycholesterol. (A)** *Gpr183*-GFP expression by the indicated mouse lung myeloid cells. Green and grey histograms show *Gpr183*-GFP expression of lung cells from *Gpr183*$^{\text{GFP/+}}$ and *Gpr183*$^{+/+}$ mice, respectively. Gating strategy for monocytes, neutrophils, and eosinophils is shown in Fig. S1 A. Dendritic cells were gated as live CD45$^+$ lineage (CD3/CD19/NK1.1)$^-$CD64$^-$Ly6G$^-$CD11c$^+$MHCII$^+$ single cells. Data are representative of greater than or equal to three independent experiments with a total of $n \geq 6$ mice per genotype. **(B)** *Gpr183*-GFP expression by lung lymphocytes from *Gpr183*$^{\text{GFP/+}}$ (green histograms) and *Gpr183*$^{+/+}$ mice (grey histograms). After gating on live CD45$^+$F4/80$^-$ single cells, B cells were gated as B220$^+$CD3$^-$ cells, CD4 T cells as B220$^-$CD3$^+$TCRβ$^+$CD4$^+$ cells, and CD8 T cells as B220$^-$CD3$^+$TCRβ$^+$CD8α$^+$ cells. Data are representative of two independent experiments with a total of $n = 6$ mice per genotype. **(C)** Chemotaxis of mouse bone marrow (BM) monocytes toward 7α,25-dihydroxycholesterol (7α,25-OHC). Left panel shows the transwell migration of bone marrow monocytes from B6 mice to the indicated concentrations of 7α,25-dihydroxycholesterol. Right panel shows the transwell migration of bone marrow monocytes from *Gpr183*$^{+/+}$ and *Gpr183*$^{-/-}$ mice to 7α,25-dihydroxycholesterol. Data are represented as mean ± SEM. *$P < 0.05$; **$P < 0.01$; ***$P < 0.001$; ****$P < 0.0001$ by one-way ANOVA with Tukey's multiple comparison post hoc test. Data are pooled from two (left panel) or three (right panel) independent experiments. Each experiment was performed with cells from one mouse per genotype and with two technical replicates per condition (total $n = 4$–6).

when bone marrow cells were differentiated into macrophages (Fig. 2 G). Like their counterparts in the lung, Ly6C$^{\text{hi}}$ bone marrow monocytes expressed *Gpr183* mRNA, and *Gpr183* expression was maintained in M-CSF–induced "generic" macrophages (Fig. 2 H). In contrast, alveolar macrophage–like cells generated in the presence of GM-CSF and TGFβ (Luo et al., 2021) had lower *Gpr183* expression, especially the CD11b$^{\text{lo}}$ subset (Fig. 2 H) that resembles resident alveolar macrophages *in vivo*. Taken together, these results show that lung macrophages in the interstitial niche express *Gpr183*, whereas monocyte-derived macrophages downregulate *Gpr183* expression when becoming resident in the alveolar niche.

Trajectory of monocyte-to-macrophage differentiation and GPR183 expression after experimental emptying of the alveolar niche

We next examined GPR183 expression during repopulation of the empty alveolar niche. For this purpose, we used a new

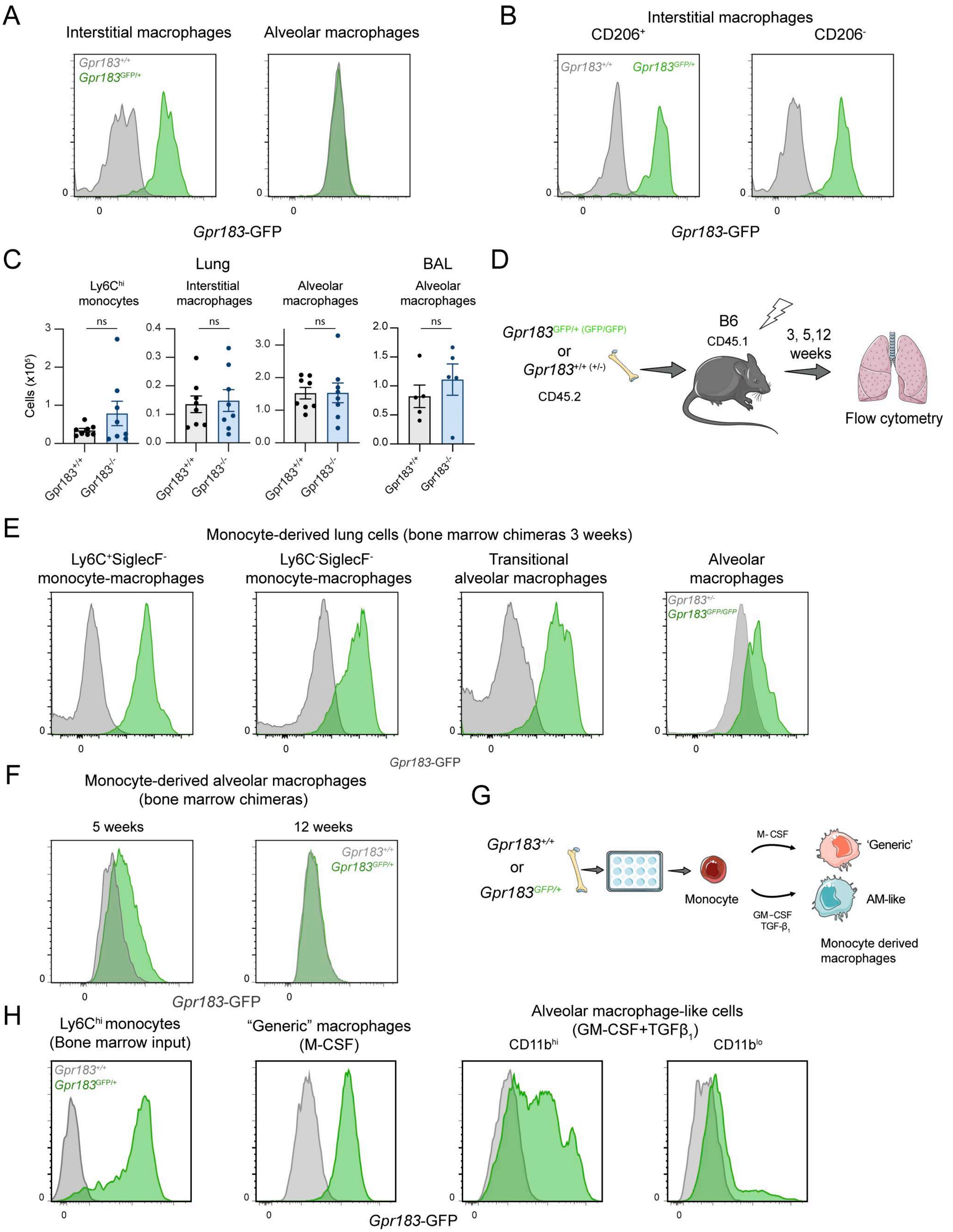

Figure 2. **Anatomical niche impacts GPR183 expression by lung macrophages. (A)** *Gpr183*-GFP expression by interstitial and alveolar macrophages from lung and BAL fluid of *Gpr183*$^{GFP/+}$ (green histograms) and *Gpr183*$^{+/+}$ mice (grey histograms), respectively. Gating strategy is shown in Fig. S1 A. Data are representative of three independent experiments with a total of *n* = 5–6 mice per genotype. **(B)** *Gpr183*-GFP expression by subsets of interstitial lung

macrophages from *Gpr183*$^{GFP/+}$ (green histograms) and *Gpr183*$^{+/+}$ mice (grey histograms). Gating strategy is shown in Fig. S1 A. Data are representative of three independent experiments with a total of *n* = 6 mice per genotype. **(C)** Number of lung monocytes and macrophages in *Gpr183*$^{+/+}$ and *Gpr183*$^{-/-}$ mice. Gating strategy is shown in Fig. S1 C. Data are represented as mean ± SEM. ns, not significant by unpaired Student's *t* test. Lung data are pooled from three independent experiments with a total of *n* = 8 mice per genotype. BAL data are pooled from two independent experiments with a total of *n* = 5 mice per genotype. **(D)** Generation of *Gpr183*$^{GFP/+}$ or *Gpr183*$^{GFP/GFP}$ (CD45.2$^+$) → B6 (CD45.1$^+$) bone marrow chimeras. *Gpr183*$^{+/+}$ or *Gpr183*$^{+/-}$ (CD45.2$^+$) → B6 (CD45.1$^+$) chimeras were used as negative controls. **(E)** *Gpr183*-GFP expression by the indicated CD45.2$^+$ monocyte–derived macrophage populations from the lung of *Gpr183*$^{GFP/GFP}$ (CD45.2$^+$) → B6 (CD45.1$^+$) bone marrow chimeras (green histograms) 3 wk after bone marrow transfer. CD45.2$^+$ macrophages from *Gpr183*$^{+/-}$ (CD45.2$^+$) → B6 (CD45.1$^+$) bone marrow chimeras (grey histograms) were used as a control. Gating strategy is shown in Fig. S1 B. Data are representative of two independent bone marrow chimera experiments with a total of *n* = 4 mice per genotype. **(F)** *Gpr183*-GFP expression by CD45.2$^+$ monocyte–derived alveolar macrophages from the BAL fluid of *Gpr183*$^{GFP/+}$ (CD45.2$^+$) → B6 (CD45.1$^+$) bone marrow chimeras (green histograms) 5 and 12 wk after bone marrow transfer. Macrophages from *Gpr183*$^{+/+}$ (CD45.2$^+$) → B6 (CD45.1$^+$) bone marrow chimeras (grey histograms) were used as a control. Gating strategy is shown in Fig. S1 A. Data are representative of two independent bone marrow chimera experiments with a total of *n* = 2–4 mice per genotype and time point. **(G)** Experimental setup to generate bone marrow–derived macrophages *in vitro*. Bone marrow cells from *Gpr183*$^{GFP/+}$ or *Gpr183*$^{+/+}$ mice were cultured with either M-CSF or GM-CSF and TGFβ$_1$ to generate generic macrophages or alveolar macrophage-like cells, respectively. **(H)** *Gpr183*-GFP expression by *in vitro*–generated macrophages from *Gpr183*$^{GFP/+}$ bone marrow cells (green histograms). Macrophages differentiated from *Gpr183*$^{+/+}$ bone marrow were used as a control (grey histograms). *Gpr183*-GFP expression by Ly6C^{hi} monocytes (bone marrow input) is shown on the left. Data are representative of two independent experiments with a total of *n* = 2 mice per genotype and two technical replicates per experiment. Panels D and G were adapted from Servier Medical Art.

mouse model, called "SPAM deleter mice" (Fig. 3 A), that allows specific depletion of alveolar macrophages in an inducible manner (Verwaerde et al., 2025). Accordingly, intratracheal diphtheria toxin (DT) administration induced the rapid depletion of resident CD11c$^+$SiglecF$^+$ alveolar macrophages that were replaced within 2 wk (Fig. 3, B and C). Alveolar macrophage depletion increased the cytokines GM-CSF and M-CSF and the chemokine CCL2 in the bronchoalveolar lavage (BAL) fluid of SPAM deleter mice within 1 day (Fig. S2, A and B). Furthermore, DT-induced alveolar macrophage depletion caused neutrophil influx into the alveolar space (Fig. 3 C) and an increase in TNFα protein, whereas amounts of IL-1α and IL-β protein were unchanged in the BAL fluid (Fig. S2, A and B).

To track the trajectory of lung monocytes during macrophage differentiation, we performed single-cell RNA sequencing of lung cells from SPAM deleter mice before and 0.5, 1, 2, 5, 8, and 14 days after DT-mediated alveolar macrophage depletion (Fig. 3 D). Uniform Manifold Approximation and Projection (UMAP) showed several clusters of non-hematopoietic cells as well as hematopoietic cells that were protected from intravascular anti-CD45 antibody labeling and therefore resident in the lung (Fig. 3 E and Fig. S2 C). Zooming in on monocyte and macrophage clusters revealed the rapid recruitment of monocytes 12 h after alveolar macrophage depletion and their timed progression toward becoming recruited alveolar macrophages (Fig. 3 F and Fig. S2, D and E). Consistent with our results in *Gpr183*$^{GFP/+}$ reporter mice (Fig. 1 A and Fig. 2, A, E, and F), *Gpr183* mRNA expression was highest in lung monocytes, interstitial lung macrophages, and differentiating monocyte-derived macrophages in SPAM deleter mice (Fig. 3 G). In contrast, resident alveolar macrophages and mature alveolar macrophages derived from recruited monocytes (on day 14 after depletion) did not express *Gpr183* (Fig. 3 G). We conclude that developing alveolar macrophages derived from monocytes express *Gpr183* mRNA during irradiation-induced lung injury and after experimental depletion of alveolar macrophages. Once the lung has returned to homeostasis and monocyte-derived alveolar macrophages have become resident, *Gpr183* expression is downregulated.

GPR183 promotes repopulation of lung macrophage niches by monocytes

Gpr183 expression in Ly6C^{hi} monocytes, known precursors of tissue-resident macrophages, led us to ask whether GPR183 was required for the differentiation of injury-induced lung macrophages. Lung injury was induced by whole-body irradiation, which causes replacement of host hematopoiesis by donor bone marrow and depletion of resident lung macrophages. We employed competitive bone marrow chimeras to study lung macrophages derived from *Gpr183*-deficient and *Gpr183*-sufficient monocytes within the same microenvironment *in vivo*. For this purpose, irradiated B6 mice (CD45.1$^+$) were reconstituted with a 1:1 mixture of *Gpr183*$^{+/+}$ (CD45.1.2$^+$) and *Gpr183*$^{-/-}$ (CD45.2$^+$) or *Gpr183*$^{+/+}$ (CD45.2$^+$) and *Gpr183*$^{-/-}$ (CD45.1.2$^+$) bone marrow cells. *Gpr183*$^{+/+}$ and *Gpr183*$^{-/-}$ Ly6C^{hi} monocytes were present at similar frequencies in blood and lung 9–13 wk after bone marrow transfer, consistent with the bone marrow input ratio (Fig. 4, A and B; and Fig. S1 C). In contrast, *Gpr183*$^{+/+}$ monocyte-derived alveolar macrophages outcompeted their *Gpr183*$^{-/-}$ counterparts at a ratio of ∼2:1 (Fig. 4, A and B; and Fig. S1 C). The skewed *Gpr183*$^{+/+}$ to *Gpr183*$^{-/-}$ ratio showed that *Gpr183*-deficient interstitial lung macrophages also had a defect in repopulating the injured lung (Fig. 4, A and B; and Fig. S1 C). Over time, *Gpr183*-deficient alveolar macrophages were progressively outcompeted (∼9:1) by their WT counterparts, as shown by flow cytometry 19–23 wk after bone marrow transfer (Fig. 4 C). We also generated single-transfer *Gpr183*$^{+/+}$ (CD45.2$^+$) → B6 (CD45.1$^+$) and *Gpr183*$^{-/-}$ (CD45.2$^+$) → B6 (CD45.1) bone marrow chimeras to assess the role of GPR183 in a noncompetitive context. These experiments showed that *Gpr183*-deficient monocytes were able to replenish an empty lung macrophage niche in the absence of cell–cell competition (Fig. 4 D). Overall, these results demonstrate that the replacement of resident lung macrophages by monocyte-derived macrophages after irradiation-induced lung injury is supported by GPR183 in a cell-intrinsic manner.

We next asked whether oxysterols sensed by the surface receptor GPR183 regulate monocyte-to-macrophage differentiation in organs other than the lung. Analysis of competitive *Gpr183*$^{+/+}$/*Gpr183*$^{-/-}$ chimeras showed that macrophage populations in the spleen, peritoneal cavity, and brain originated

https://doi.org/10.1084/jem.20252667

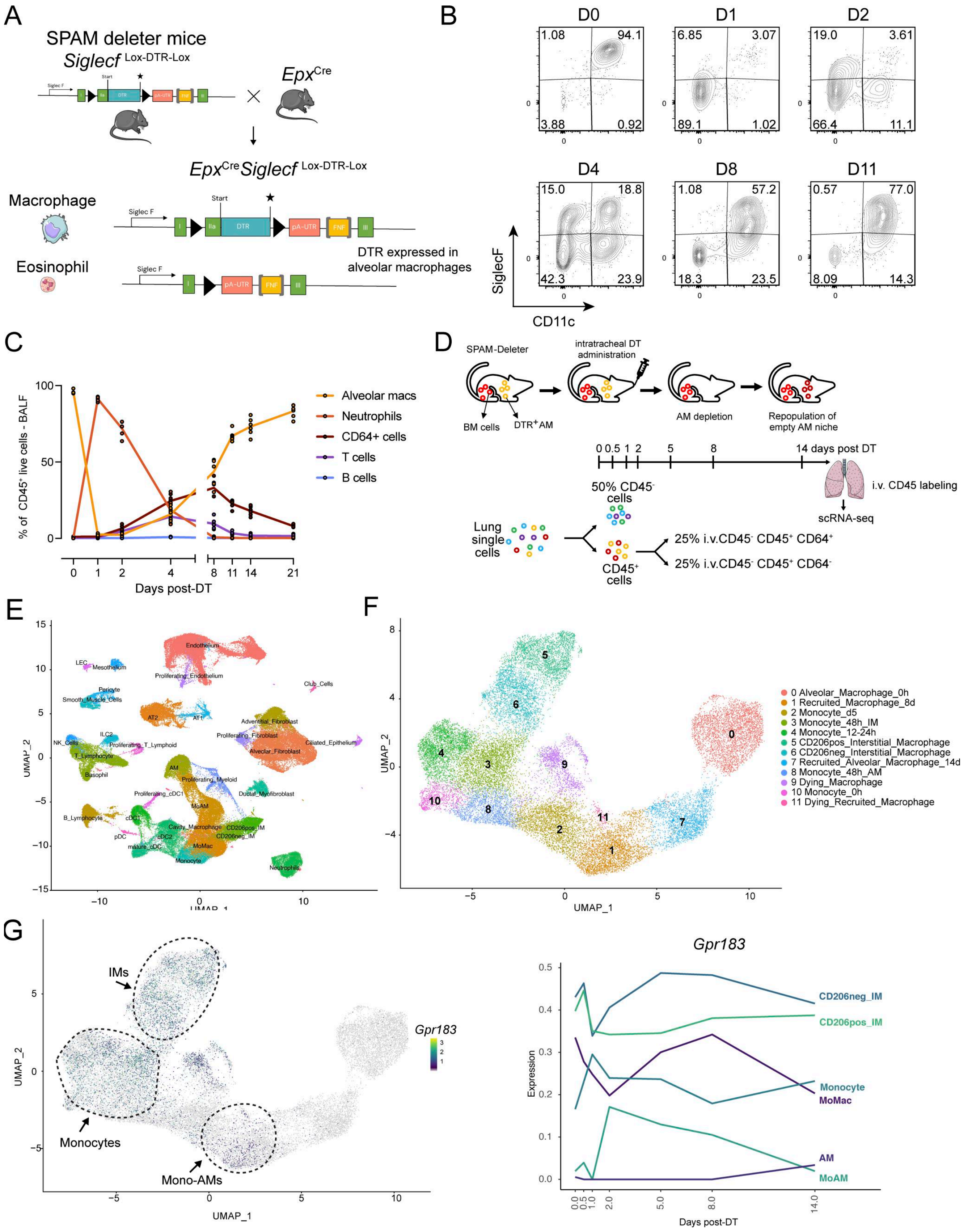

Figure 3. **Trajectory of monocyte-to-macrophage differentiation and GPR183 expression after experimental emptying of the alveolar niche. (A)** Overview of SPAM deleter mice. In *Siglecf*$^{\text{Lox-DTR-Lox}}$ mice, SiglecF^{+} alveolar macrophages and eosinophils express DTR. In *Epx*$^{\text{Cre}}$ *Siglecf*$^{\text{Lox-DTR-Lox}}$ mice (SPAM deleter mice), *Epx*$^{\text{Cre}}$ activity excises the floxed DTR cassette in eosinophils, resulting in alveolar macrophage–specific DTR expression. This allows

specific depletion of alveolar macrophages in an inducible manner after DT administration. **(B and C)** Frequency of alveolar macrophages and other immune cells in the BAL fluid (BALF) of SPAM deleter mice after intratracheal administration of 100 pg DT as determined by flow cytometry. BAL cells in panel B were gated as live CD45$^+$ single cells. Myeloid cells in panel C were gated by excluding CD11b$^-$CD11c$^-$ cells and were further separated into alveolar macrophages (CD11c$^+$SiglecF$^+$), CD64$^+$ non-alveolar macrophages (CD11c$^-$SiglecF$^-$CD64$^+$), and neutrophils (CD11c$^-$SiglecF$^-$CD11b$^+$Ly6G$^+$). Nonmyeloid cells (CD11b$^-$CD11c$^-$) were separated into T (CD3$^+$B220$^-$) and B cells (CD3$^-$B220$^+$). Alveolar macs, alveolar macrophages. Data are from a single experiment with *n* = 5–6 mice per time point. **(D)** Experimental setup for single-cell RNA sequencing of lung cells from SPAM deleter mice. Lungs were harvested at the indicated time points before and after alveolar macrophage depletion with 40 ng intratracheal DT. Purified CD45$^-$ non-hematopoietic cells as well as resident CD45$^+$CD64$^+$ and CD45$^+$CD64$^-$ hematopoietic cells were used for single-cell RNA sequencing as described in the Materials and methods. Resident hematopoietic cells were isolated based on being protected from intravascular cell labeling after intravenous injection of anti-mouse CD45 antibody. AM, alveolar macrophages. **(E)** Combined UMAP of 117,715 lung cells from SPAM deleter mice at 0, 12, 24, and 48 h and on day 5, 8, and 14 after alveolar macrophage depletion with DT as determined by single-cell RNA sequencing. See Fig. S2 C for markers used to annotate the cell clusters. **(F)** UMAP showing monocyte and macrophage clusters (26,817 cells) in the lung of SPAM deleter mice before and after alveolar macrophage depletion with DT. See Fig. S2 D for markers used to annotate the monocyte-macrophage clusters. **(G)** *Gpr183* expression in the monocyte and macrophage clusters from panel F. IMs, interstitial macrophages; MoMac, monocyte-macrophages; MoAM or mono-AMs, monocyte-derived alveolar macrophages. Data in panels E–G are from one single-cell RNA-sequencing experiment with *n* = 4 mice per time point. Panels A and D were adapted from Servier Medical Art.

---

equally from *Gpr183*$^{+/+}$ and *Gpr183*$^{-/-}$ bone marrow monocytes (Fig. 4 E and Fig. S3, A–D). The lower *Gpr183*$^{+/+}$ to *Gpr183*$^{-/-}$ ratios indicated that GPR183 may inhibit rather than promote the development of monocyte-derived macrophages in the liver (Fig. 4 E and Fig. S3 E). We conclude that GPR183 predominantly promotes monocyte-to-macrophage differentiation in the lung.

To confirm these findings in models without genotoxic lung injury, we performed mixed bone marrow chimeras in SPAM deleter mice and in IM-DT receptor (DTR) (*Tmem119*$^{\mathrm{Cre}}$ *Cx3cr1*$^{\mathrm{LSL\text{-}DTR}}$) mice that allow the inducible depletion of interstitial lung macrophages by DT (Vanneste et al., 2023). First, SPAM deleter mice (CD45.2$^+$) were reconstituted with a 1:1 mixture of *Gpr183*$^{+/+}$ or *Gpr183*$^{-/-}$ (CD45.1.2$^+$) and B6 (CD45.1$^+$) bone marrow cells. SPAM deleter recipients were treated with busulfan to replace host monocytes while preserving host alveolar macrophages (Misharin et al., 2017) before depleting them with DT 7 wk after bone marrow transfer (Fig. 5 A). Analysis at 4 wk after DT administration revealed that macrophages derived from *Gpr183*$^{+/+}$ bone marrow were more efficient than their *Gpr183*$^{-/-}$ counterparts at repopulating the alveolar niche (Fig. 5, A and B). In contrast, *Gpr183*$^{+/+}$ and *Gpr183*$^{-/-}$ bone marrow cells contributed equally to Ly6C$^{\mathrm{hi}}$ monocytes in the blood and lung (Fig. 5 B). Second, we employed a similar approach to determine whether *Gpr183* was required for repopulating the interstitial lung macrophage niche. In thorax-shielded IM-DTR bone marrow chimeras (Fig. 5 C), the ratio of *Gpr183*$^{-/-}$ to B6 interstitial lung macrophages was significantly lower than the ratio of *Gpr183*$^{+/+}$ to B6 interstitial lung macrophages 2 wk after DT administration (Fig. 5, C and D). Therefore, *Gpr183*-deficient monocytes had a reduced ability to fill the vacant interstitial macrophage niche. Ly6C$^{\mathrm{hi}}$ blood monocytes were not impacted by the absence of *Gpr183*, whereas *Gpr183*$^{+/+}$ bone marrow cells were more efficient at reconstituting Ly6C$^{\mathrm{hi}}$ lung monocytes in IM-DTR mice (Fig. 5 D). We conclude that GPR183 promotes the replenishment of alveolar and interstitial macrophage niches by bone marrow–derived monocytes.

Energy metabolism controls macrophage homeostasis and alveolar macrophages are dependent on oxidative phosphorylation (Wculek et al., 2023). However, we found that GPR183 was dispensable for homeostatic alveolar macrophage metabolism because, like their *Gpr183*$^{+/+}$ counterparts, *Gpr183*-deficient alveolar macrophages derived from monocytes in competitive *Gpr183*$^{+/+}$/*Gpr183*$^{-/-}$ bone marrow chimeras were mainly fueled by oxidative phosphorylation (Fig. S4 A). Finally, we examined the impact of GPR183 on monocyte-to-macrophage differentiation *in vitro*. Congenically marked *Gpr183*$^{+/+}$ and *Gpr183*$^{-/-}$ bone marrow cells were mixed 1:1 and cultured with either M-CSF or GM-CSF and TGFβ$_1$ in the absence or presence of the GPR183 ligand 7α,25-dihydroxycholesterol (Fig. S4 B). An equal *Gpr183*$^{+/+}$ to *Gpr183*$^{-/-}$ ratio of macrophages was maintained in all culture conditions (Fig. S4, B and C). These data demonstrate that genetic deletion of *Gpr183* does not cause a general defect in macrophage differentiation per se.

Cell type–specific requirement of GPR183 expression for monocyte-derived alveolar macrophages

Since B and T cells also expressed *Gpr183* (Fig. 1 B), we asked whether lymphocyte-expressed GPR183 contributes to promoting the development of monocyte-derived alveolar macrophages. To address this possibility, irradiated B6 (CD45.1$^+$) recipient mice were transplanted with *Rag1*$^{-/-}$ (CD45.2$^+$) bone marrow mixed with either *Gpr183*$^{+/+}$ or *Gpr183*$^{-/-}$ (CD45.1.2$^+$) bone marrow (Fig. 6 A). In mixed *Gpr183*$^{-/-}$/*Rag1*$^{-/-}$ chimeras, *Gpr183* is expressed only in innate immune cells, whereas T and B lymphocytes lack *Gpr183*. As in competitive *Gpr183*$^{+/+}$/*Gpr183*$^{-/-}$ bone marrow chimeras (Fig. 4 B), *Gpr183*-deficient alveolar macrophages were outcompeted in mixed *Gpr183*/*Rag1*$^{-/-}$ chimeras by their *Gpr183*-sufficient counterparts (Fig. 6 B). This result indicated that *Gpr183* expression in innate immune cells supports monocyte-to-alveolar macrophage differentiation. To address whether GPR183 expression by monocytes promotes their differentiation into alveolar macrophages, we created mixed *Gpr183*$^{+/+}$ (CD45.1.2$^+$)/*Ccr2*$^{\mathrm{RFP/RFP}}$(CD45.2$^+$) and *Gpr183*$^{-/-}$ (CD45.1.2$^+$)/*Ccr2*$^{\mathrm{RFP/RFP}}$(CD45.2$^+$) bone marrow chimeras in B6 (CD45.1$^+$) recipients (Fig. 6 C). CCR2 is required for monocyte egress from bone marrow into the blood (Serbina and Pamer, 2006). Therefore, lung monocytes in mixed *Gpr183*$^{-/-}$/*Ccr2*$^{\mathrm{RFP/RFP}}$ chimeras do not express *Gpr183*, whereas *Gpr183* expression in other cells is preserved. The similar ratio of *Gpr183*$^{+/+}$/*Ccr2*$^{\mathrm{RFP/RFP}}$ and *Gpr183*$^{-/-}$/*Ccr2*$^{\mathrm{RFP/RFP}}$ alveolar macrophages (Fig. 6 D) suggested that *Gpr183* expression in CCR2$^+$ monocytes is required to

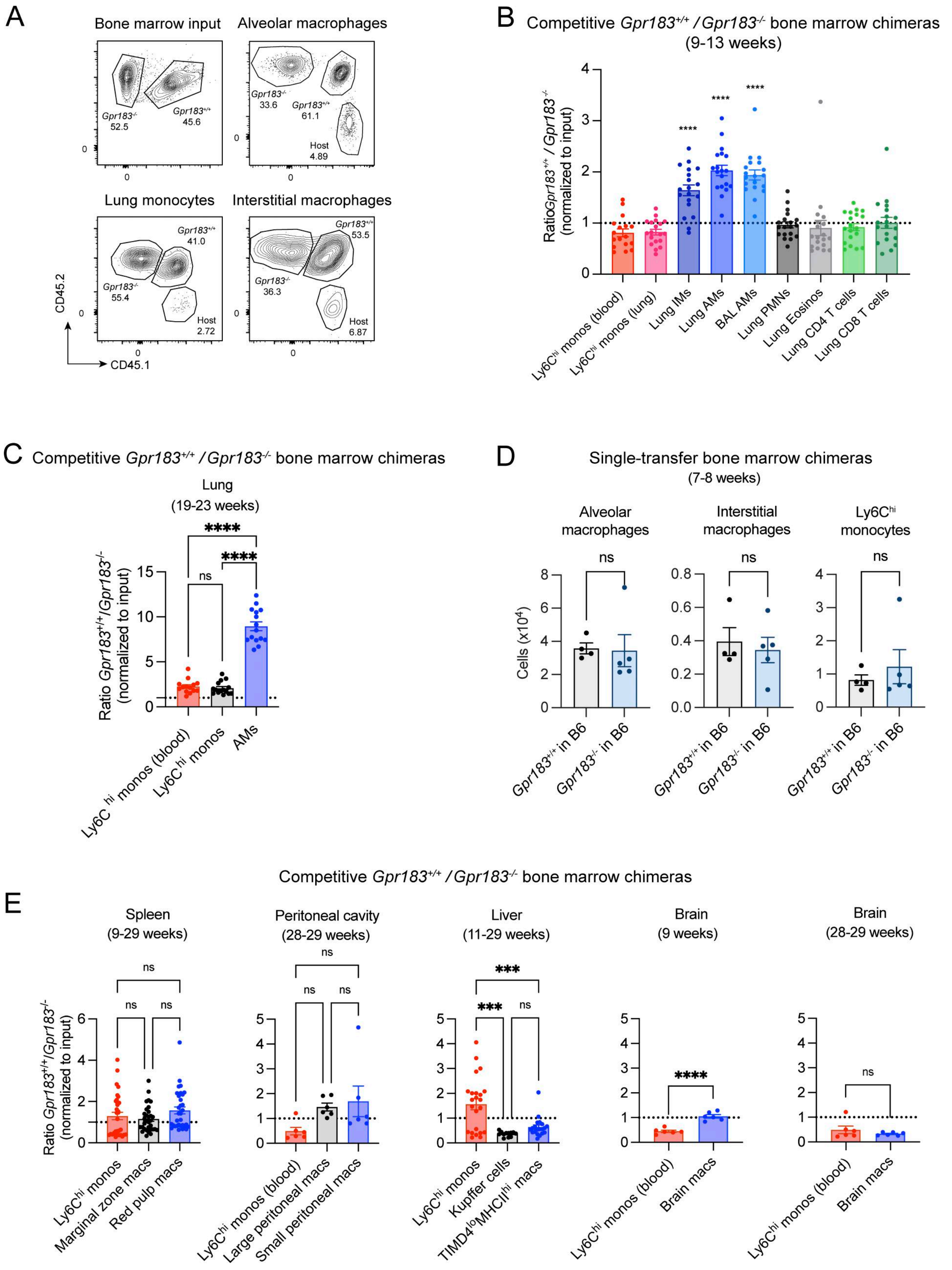

Figure 4. **GPR183 promotes the development of monocyte-derived macrophages in the lung. (A and B)** Chimerism of monocytes, alveolar macrophages, interstitial macrophages, and other lung immune cells in competitive *Gpr183*$^{+/+}$/*Gpr183*$^{-/-}$ chimeras 9–13 wk after bone marrow transfer. Injected bone marrow input is shown in the upper left flow cytometry dot plot of panel A. Gating strategy is shown in Fig. S1 C. The ratio of the indicated *Gpr183*$^{+/+}$/*Gpr183*$^{-/-}$ cells in panel B was normalized to the bone marrow input of each independent chimera experiment. AMs, alveolar macrophages; IMs, interstitial macrophages; PMNs,

polymorphonuclear neutrophils. Data are represented as mean ± SEM. ****P < 0.0001 by one-way ANOVA with Tukey's multiple comparison post hoc test. Data are pooled from three independent bone marrow chimera experiments with a total of *n* = 17–19 mice. **(C)** Chimerism of Ly6C^{hi} monocytes and alveolar macrophages in the lung of competitive *Gpr183*$^{+/+}$/*Gpr183*$^{-/-}$ chimeras 19–23 wk after bone marrow transfer. Gating strategy is shown in Fig. S1 C. The ratio of the indicated *Gpr183*$^{+/+}$/*Gpr183*$^{-/-}$ cells was normalized to the bone marrow input of each independent chimera experiment. Data are represented as mean ± SEM. ns, not significant; ****P < 0.0001 by one-way ANOVA with Tukey's multiple comparison post hoc test. Data are pooled from two independent bone marrow chimera experiments with a total of *n* = 14–15 mice. **(D)** Number of CD45.2$^+$ lung monocytes and macrophages in single-transfer *Gpr183*$^{+/+}$ (CD45.2$^+$) → B6 (CD45.1$^+$) and *Gpr183*$^{-/-}$ (CD45.2$^+$) → B6 (CD45.1$^+$) chimeras 7–8 wk after bone marrow transfer. Gating strategy is shown in Fig. S1 C. Data are represented as mean ± SEM. ns, not significant by unpaired Student's *t* test. Data are pooled from two independent experiments from a single bone marrow chimera experiment with a total of *n* = 4–5 mice per genotype. **(E)** Chimerism of Ly6C^{hi} monocytes and macrophages in the indicated tissues of competitive *Gpr183*$^{+/+}$/*Gpr183*$^{-/-}$ chimeras 9–29 wk after bone marrow transfer. Macs, macrophages; monos, monocytes. Gating strategy is shown in Fig. S3. Data are represented as mean ± SEM. ns, not significant; ***P < 0.001; ****P < 0.0001 by one-way ANOVA with Tukey's Multiple Comparison post hoc test (spleen, peritoneal cavity, and liver) or by unpaired Welch's *t* test (brain). Data are pooled from one (peritoneal cavity), three (brain), four (liver), or five (spleen) independent bone marrow chimera experiments with a total of *n* = 6–32 mice per tissue.

---

confer a competitive advantage for monocyte-to-alveolar macrophage differentiation.

GPR183 supports the early stages of monocyte-to-lung macrophage differentiation

To further examine the role of GPR183 in lung macrophage differentiation, we analyzed competitive *Gpr183*$^{+/+}$/*Gpr183*$^{-/-}$ chimeras at 3 wk after bone marrow reconstitution (Fig. 7 A). The normal *Gpr183*$^{+/+}$ to *Gpr183*$^{-/-}$ ratios of Ly6C^{hi} monocytes in bone marrow and blood demonstrated that GPR183 was dispensable for monopoiesis and monocyte egress into the circulation (Fig. 7 B). During lung macrophage differentiation, monocytes first upregulate CD64 before downregulating Ly6C, which is then followed by the upregulation of CD11c and finally SiglecF surface expression (Li et al., 2022a; Ruscitti et al., 2024; Sabatel et al., 2017). Consistent with this notion, lung tissue of the *Gpr183*$^{+/+}$/*Gpr183*$^{-/-}$ chimeras at 3 wk contained CD64$^+$CD11b$^+$Ly6C$^+$SiglecF$^-$ and CD64$^+$CD11b$^+$Ly6C$^-$SiglecF$^-$ monocyte-macrophages, as well as CD64$^+$CD11c$^+$SiglecF^{lo-mid} transitional alveolar macrophages (Fig. 7, A and B; and Fig. S1 B). We found that bone marrow–derived *Gpr183*$^{+/+}$ cells started to outcompete their *Gpr183*$^{-/-}$ counterparts from the CD64$^+$CD11b$^+$Ly6C$^+$SiglecF$^-$ monocyte-macrophage stage, whereas Ly6C^{hi}CD64$^-$ lung monocytes originated equally from *Gpr183*$^{+/+}$ and *Gpr183*$^{-/-}$ bone marrow (Fig. 7, A and B). These data show that lack of GPR183 leads to a defect in early monocyte-to-lung macrophage differentiation.

GPR183 ligand produced by non-hematopoietic cells is required for monocyte-to-lung macrophage differentiation

Next, we determined the cellular source of the GPR183 ligand 7α,25-dihydroxycholesterol in the injured lung. First, we asked whether *Ch25h*-dependent generation of 7α,25-dihydroxycholesterol promotes reconstitution of the lung macrophage compartment by monocytes. To address this question, irradiated *Ch25h*$^{+/+}$ or *Ch25h*$^{-/-}$ (CD45.2$^+$) mice were reconstituted with an equal mixture of *Gpr183*$^{+/+}$ or *Gpr183*$^{-/-}$ (CD45.1.2$^+$) and B6 (CD45.1$^+$) bone marrow (Fig. 7 C). In *Ch25h*-sufficient hosts, alveolar and interstitial lung macrophages derived from *Gpr183*$^{+/+}$ bone marrow outcompeted their *Gpr183*$^{-/-}$-derived counterparts ~twofold after bone marrow transfer (Fig. 7 C), consistent with our results above (Fig. 4, A and B). In contrast, the competitive disadvantage of *Gpr183*$^{-/-}$ lung macrophages was not observed in a *Ch25h*-deficient microenvironment (Fig. 7 C). These findings demonstrate that a radioresistant source of *Ch25h* is required for the GPR183-dependent repopulation of macrophage niches after lung injury. To confirm that *Ch25h* was predominantly expressed by radioresistant cells in the injured lung, we used bone marrow chimeras with either *Ch25h*$^{+/+}$ or *Ch25h*$^{-/-}$ bone marrow donors and recipients (Fig. 7 D). We found that *Ch25h* mRNA expression in the lung was similar in irradiated *Ch25h*$^{+/+}$ hosts injected with either *Ch25h*$^{+/+}$ or *Ch25h*$^{-/-}$ bone marrow (Fig. 7 D). In contrast, *Ch25h*$^{-/-}$ hosts failed to support normal *Ch25h* mRNA expression in the lung 3–4 wk after bone marrow injection. These results showed that *Ch25h* in the injured lung is mainly derived from non-hematopoietic (radioresistant) cells. Taken together, these data show that a non-hematopoietic source of the GPR183 ligand 7α,25-dihydroxycholesterol supports the development of monocyte-derived lung macrophages.

Fibroblasts are the main source of GPR183 ligand-producing enzymes in the lung

To further define the cellular source of 7α,25-dihydroxycholesterol, we leveraged our single-cell RNA-sequencing data from SPAM deleter mice (Fig. 3, D and E). Given the radioresistant source of 7α,25-dihydroxycholesterol (Fig. 7, C and D), we focused on expression of enzymes regulating 7α,25-dihydroxycholesterol production in non-hematopoietic cell clusters. We reasoned that cells co-expressing *Ch25h* and *Cyp7b1* are the main producers of 7α,25-dihydroxycholesterol. We found that lung fibroblasts expressed both *Ch25h* and *Cyp7b1* with alveolar fibroblasts having the highest expression (Fig. 8 A and Fig. S2 C). Time course analysis showed that expression of *Ch25h* and especially *Cyp7b1* in the lung of SPAM deleter mice was rapidly upregulated after alveolar macrophage depletion (Fig. 8 B). In contrast, the 7α,25-dihydroxycholesterol-degrading enzyme *Hsd3b7* was downregulated (Fig. 8 B). These results are consistent with increased production of the GPR183 ligand 7α,25-dihydroxycholesterol after alveolar macrophage depletion. The peak of *Cyp7b1* mRNA expression at 48 h after alveolar macrophage depletion (Fig. 8 B) coincided with the time point when recruited monocytes began to differentiate into alveolar macrophages (Fig. 3 B, C, and F; and Fig. S2, D and E). Further analysis demonstrated that fibroblasts upregulated both *Ch25h* and *Cyp7b1* expression within 12 h after alveolar macrophage depletion (Fig. 8, C and D).

We confirmed these findings in the context of monocyte-to-interstitial lung macrophage differentiation using the IM-DTR model (Fig. 8, E and F). Single-cell RNA sequencing of niche cells

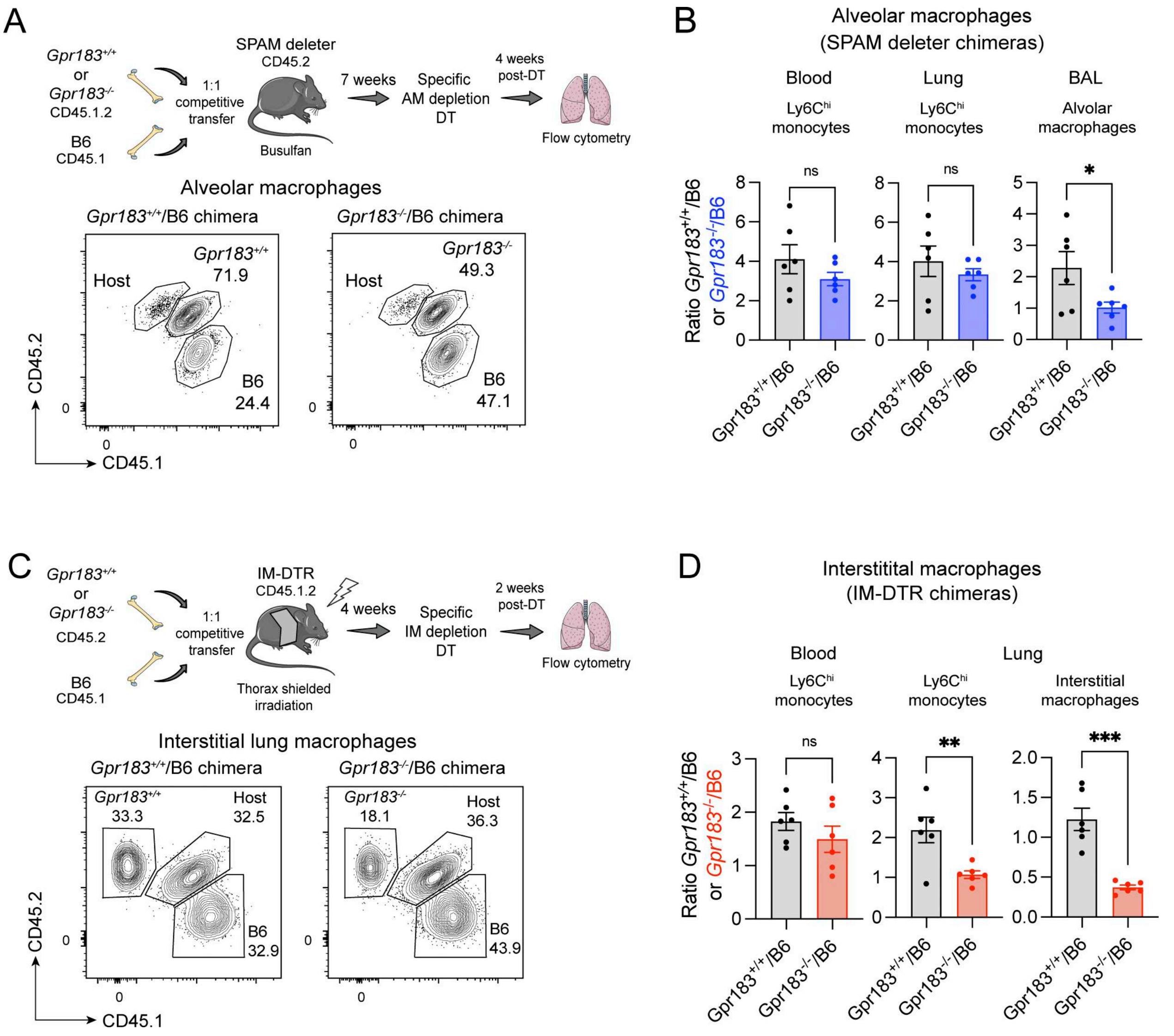

Figure 5. **GPR183 promotes repopulation of lung macrophage niches by monocytes. (A and B)** Chimerism of *Gpr183*$^{+/+}$ and *Gpr183*$^{-/-}$ blood monocytes, lung monocytes, and alveolar macrophages from SPAM deleter mice 7 wk after bone marrow reconstitution and 4 wk after depletion of alveolar macrophages with 1 ng intratracheal DT. Data are represented as mean ± SEM. ns, not significant; $^{*}P < 0.05$ by unpaired Student's *t* test. Data are pooled from two independent bone marrow chimera experiments with a total of $n = 6$ mice per genotype. **(C and D)** Chimerism of *Gpr183*$^{+/+}$ and *Gpr183*$^{-/-}$ blood monocytes, lung monocytes, and interstitial macrophages in the lung of IM-DTR deleter mice 4 wk after bone marrow reconstitution and 2 wk after depletion of interstitial macrophages with 50 ng intraperitoneal DT. Data are represented as mean ± SEM. ns, not significant; $^{**}P < 0.01$; $^{***}P < 0.001$; by unpaired Student's *t* test. Data are pooled from two independent bone marrow chimera experiments with a total of $n = 6$ mice per genotype. Panels A and C were adapted from Servier Medical Art. IM, interstitial macrophage.

showed that lung fibroblasts were the main non-hematopoietic cell type co-expressing *Ch25h* and *Cyp7b1* (Fig. 8 G and Fig. S5 A). In contrast, mRNA expression of the GPR183 ligand-degrading enzyme *Hsd3b7* was very low in fibroblasts, endothelial cells, and epithelial cells (Fig. 8 G). DT-induced depletion of interstitial lung macrophages triggered a rapid increase in *Ch25h* and *Cyp7b1* expression by fibroblasts with a peak at 12–24 h (Fig. 8 H). These results further support the concept that the GPR183 ligand 7α,25-dihydroxycholesterol is produced by lung fibroblasts in response to resident macrophage depletion.

We next asked whether *Ch25h*$^{+}$*Cyp7b1*$^{+}$ fibroblasts also produce known factors that induce monocyte-to-macrophage differentiation. Analysis of the SPAM deleter single-cell RNA-sequencing data showed that *Ccl2* mRNA expression increased rapidly after alveolar macrophage depletion (Fig. S5 B). CCR2, the receptor for CCL2, is required for the generation of monocyte-derived alveolar macrophages (Sabatel et al., 2017). Together with interstitial lung macrophages and monocytes, fibroblasts contributed to the peak of *Ccl2* expression at 12 h after alveolar macrophage depletion (Fig. S5 B). Expression of *Csf1*, encoding M-CSF, the critical factor for monocyte-to-lung macrophage differentiation (Aegerter et al., 2022), showed a similar upregulation after alveolar macrophage depletion (Fig. S5 C). *Csf1* mRNA expression was highest in neutrophils, but fibroblasts also expressed it (Fig. S5 C). Depletion of interstitial lung macrophages in the IM-DTR model also triggered *Csf1*

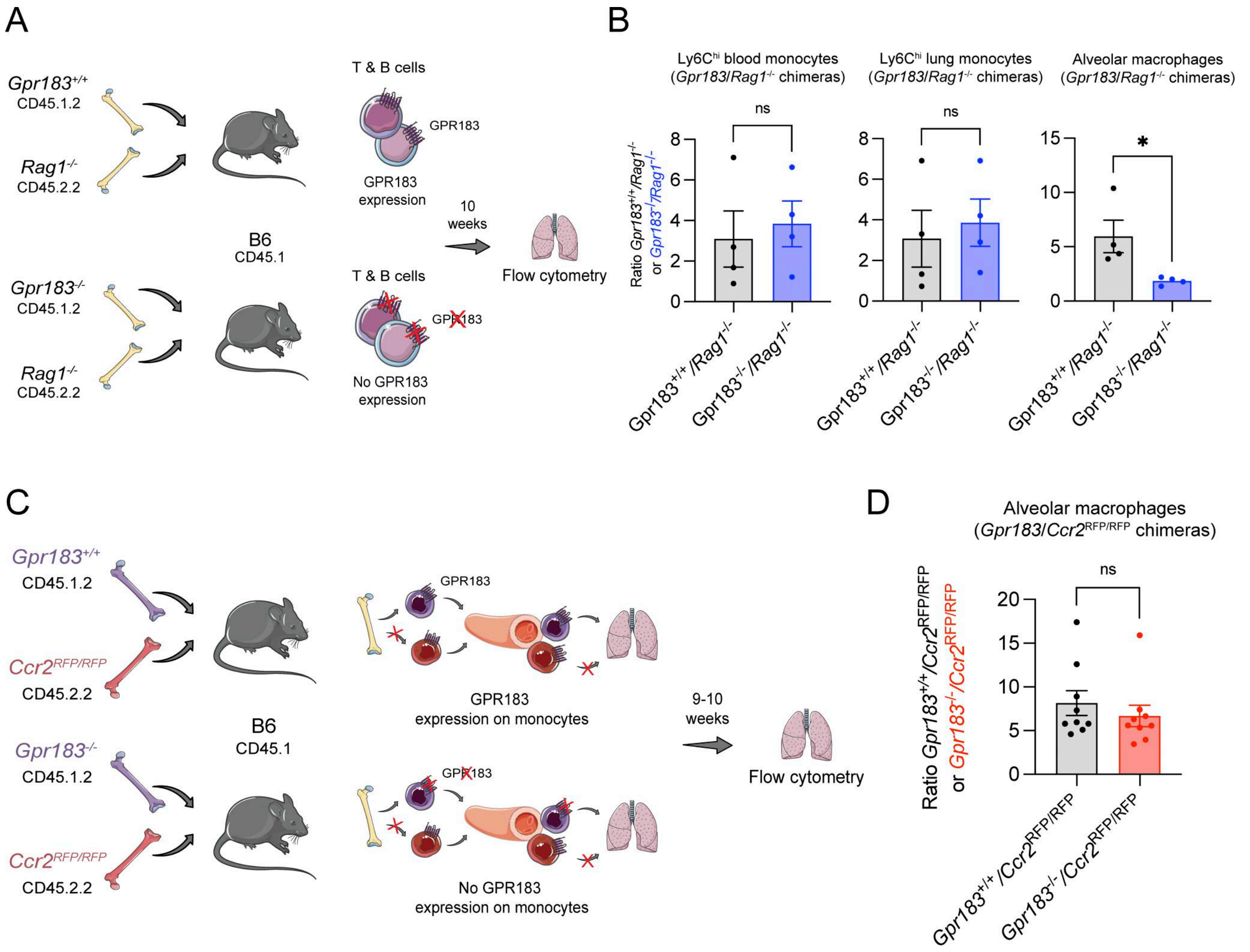

Figure 6. **Cell type–specific requirement of GPR183 expression for monocyte-derived alveolar macrophages. (A)** Overview of mixed *Gpr183*$^{+/+}$/*Rag1*$^{-/-}$ and *Gpr183*$^{-/-}$/*Rag1*$^{-/-}$ bone marrow chimeras. In mixed *Gpr183*$^{-/-}$/*Rag1*$^{-/-}$ chimeras, lymphocytes (T and B cells) lack *Gpr183* expression, whereas in control *Gpr183*$^{+/+}$/*Rag1*$^{-/-}$ chimeras *Gpr183* expression is preserved in T and B lymphocytes. **(B)** Chimerism of donor-derived monocytes and alveolar macrophages in mixed *Gpr183*$^{+/+}$/*Rag1*$^{-/-}$ and *Gpr183*$^{-/-}$/*Rag1*$^{-/-}$ chimeras 10 wk after bone marrow transfer. Gating strategy is shown in Fig. S1 C. Data are represented as mean ± SEM. ns, not significant; $^{*}P < 0.05$ by unpaired Student's *t* test. Data are pooled from two independent bone marrow chimera experiments with a total of $n = 4$ mice per genotype. **(C)** Overview of mixed *Gpr183*$^{+/+}$/*Ccr2*$^{RFP/RFP}$ and *Gpr183*$^{-/-}$/*Ccr2*$^{RFP/RFP}$ bone marrow chimeras. Monocytes derived from *Ccr2*$^{RFP/RFP}$ bone marrow have defective bone marrow egress and therefore lung monocytes in mixed *Gpr183*$^{-/-}$/*Ccr2*$^{RFP/RFP}$ chimeras lack *Gpr183* expression. **(D)** Chimerism of donor-derived alveolar macrophages in mixed *Gpr183*$^{+/+}$/*Ccr2*$^{RFP/RFP}$ and *Gpr183*$^{-/-}$/*Ccr2*$^{RFP/RFP}$ chimeras 9–10 wk after bone marrow transfer. Gating strategy is shown in Fig. S1 C. Data are represented as mean ± SEM. ns, not significant by unpaired Student's *t* test. Data are pooled from two independent bone marrow chimera experiments with a total of $n = 9$ mice per genotype. Panels A and C were adapted from Servier Medical Art.

upregulation in fibroblasts (Fig. 8 H). Taken together, our results support the notion that lung fibroblasts provide the GPR183 ligand 7α,25-dihydroxycholesterol as well as chemokines and cytokines to induce the differentiation of GPR183^{+} monocytes into lung macrophages.

GPR183-expressing monocytes interact with *Ch25h*$^{+}$ lung fibroblasts

The preferential expression of GPR183 ligand-synthesizing enzymes by lung fibroblasts predicted that *Ch25h*$^{+}$*Cyp7b1*$^{+}$ fibroblasts attract monocytes via GPR183 to a niche in the lung where monocyte-to-macrophage differentiation occurs. To test this prediction, we took advantage of *Gpr183*$^{GFP/+}$*Ch25h*^{tdTom} double reporter mice to visualize *Gpr183*$^{+}$ monocytes and *Ch25h*$^{+}$ cells in the steady-state lung and on day 3 after LPS-induced acute lung injury (Fig. 9 A). Immunofluorescence microscopy showed that platelet-derived growth factor receptor α (PDGFRα)$^{+}$ fibroblasts expressed *Ch25h*-Tomato (Fig. 9, B and C) and were closer to CD68^{+}MHCII^{-} monocytes and CD68^{+}MHCII^{+} macrophages that expressed *Gpr183*-GFP (Fig. 9, B–D), consistent with a preferential interaction between receptor-expressing and ligand-producing cells. The proximity between *Gpr183*$^{+}$ monocytes or macrophages and *Ch25h*$^{+}$ fibroblasts further increased after LPS-induced acute lung injury (Fig. 9 D). Overall, these results identify a niche in the lung where GPR183-expressing monocytes and macrophages interact with *Ch25h*$^{+}$ fibroblasts.

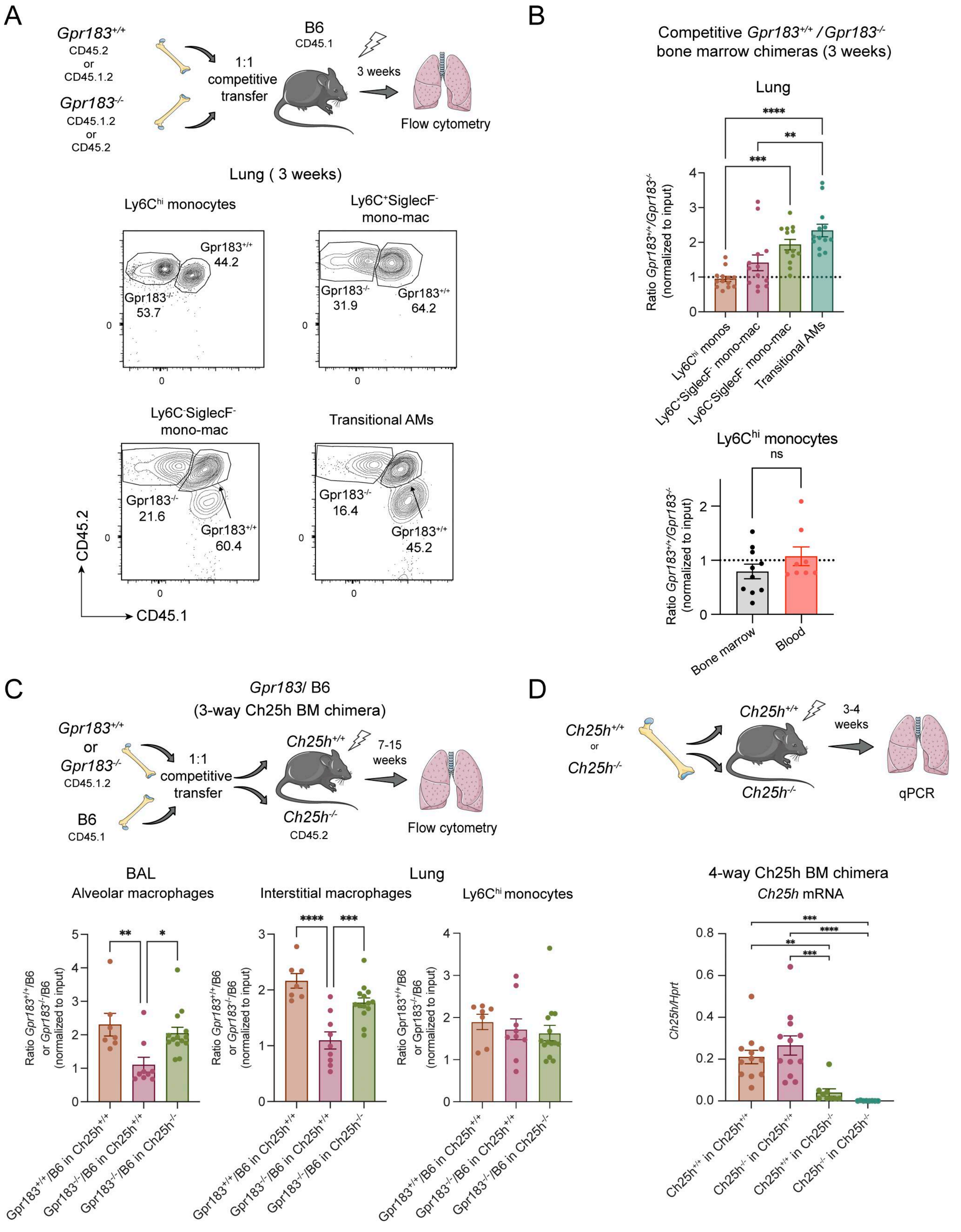

Figure 7. **GPR183 supports the early stages of monocyte-to-lung macrophage differentiation, and GPR183 ligand produced by non-hematopoietic cells is required for monocyte-to-lung macrophage differentiation. (A and B)** Chimerism of donor-derived monocytes and macrophages in bone marrow, blood, and lung of competitive *Gpr183*$^{+/+}$/*Gpr183*$^{-/-}$ chimeras 3 wk after bone marrow transfer. Gating strategy is shown in Fig. S1 B. The ratio of the indicated

Gpr183$^{+/+}$/*Gpr183*$^{-/-}$ cells was normalized to the bone marrow input of each independent chimera experiment. AMs, alveolar macrophages; BM, bone marrow; mono-mac, monocyte-macrophages; monos, monocytes. Data are represented as mean ± SEM. ns, not significant; $^{**}P < 0.01$; $^{***}P < 0.001$; $^{****}P < 0.0001$ by one-way ANOVA with Tukey's multiple comparison post hoc test (upper graph in panel B) or by unpaired Student's *t* test (lower graph in panel B). Data are pooled from three (Ly6C^{hi} monocytes in bone marrow and blood) or four (monocytes and macrophages in lung) independent bone marrow chimera experiments with a total of $n = 8–13$ mice per genotype. **(C)** Chimerism of alveolar and interstitial macrophages in the indicated *Gpr183*$^{+/+}$/B6 or *Gpr183*$^{-/-}$/B6 → *Ch25h*$^{+/+}$ or *Ch25h*$^{-/-}$ bone marrow chimeras 7–15 wk after bone marrow transfer. Gating strategy is shown in Fig. S1 C. The ratio of the indicated *Gpr183*$^{+/+}$/B6 or *Gpr183*$^{-/-}$/B6 cells was normalized to the bone marrow input of each independent chimera experiment. Data are represented as mean ± SEM. $^{*}P < 0.05$; $^{**}P < 0.01$; $^{***}P < 0.001$; $^{****}P < 0.0001$ by one-way ANOVA with Tukey's multiple comparison post hoc test. Data are pooled from two independent bone marrow chimera experiments with a total of $n = 7–14$ mice per genotype. **(D)** *Ch25h* mRNA expression in the lung of the indicated chimeras 3–4 wk after bone marrow transfer. Data are represented as mean ± SEM. $^{**}P < 0.01$; $^{***}P < 0.001$; $^{****}P < 0.0001$ by one-way ANOVA with Tukey's multiple comparison post hoc test. Data are pooled from four independent bone marrow chimera experiments with a total of $n = 8–12$ mice per genotype. Panels A, C, and D were adapted from Servier Medical Art.

Single-cell RNA sequencing identifies *GPR183*-expressing monocytes in human airway disease

To validate our findings in the human context, we investigated monocyte-derived macrophages in bronchiectasis, a structural airway disease characterized by irreversible dilatation of the bronchi and recurrent lung inflammation (Chalmers et al., 2018). For this purpose, we performed single-cell RNA sequencing of CD45^{+}CD66^{-} BAL cells (excluding neutrophils) from six bronchiectasis patients (Table S1) and integrated our single-cell RNA-sequencing data with a dataset from BAL fluid of 10 healthy donors (Mould et al., 2021). UMAP analysis showed 11 transcriptionally distinct clusters, composed of myeloid cells as well as T and B lymphocytes (Fig. 10 A). Cells in cluster 0, 2, 4, 6, and 11 (Fig. 10 A) were identified as alveolar macrophages based on expression of the master transcription factor *PPARG* (Fig. 10 B) and their high gene signature similarity score (Fig. 10 C). Cluster 1 and 10 showed greater similarity to CD14^{+} lung monocytes (Fig. 10 C) and expressed the monocyte-related transcription factor *KLF4* (Fig. 10 B). Cluster 10 was defined as *GPR183*-monocytes based on differential expression of *GPR183* (Fig. 10 B).

To further track macrophage origin in bronchiectasis, we performed gene module score analysis, taking advantage of our previous work that established the gene signatures of human lung macrophages of fetal versus monocytic origin in humanized MISTRG mice (Evren et al., 2022). The gene signatures of macrophages in cluster 0, 2, 4, 6, and 11 were most similar to that of human lung macrophages derived from CD116^{+} fetal precursors (Fig. 10 D). In contrast, cluster 1 and 10 (*GPR183*-monocytes) had lower similarity to fetal-derived lung macrophages and a higher gene module score for hematopoietic stem and progenitor cell (HSPC)-derived lung macrophages (Fig. 10 D), consistent with a monocytic origin. *GPR183*-monocytes (cluster 10) and monocytic *VCAN*-macrophages (cluster 1) as well as T lymphocytes (clusters 3 and 5) were expanded in bronchiectasis compared with healthy airways (Fig. 10 E). Finally, we used the Slingshot algorithm (Street et al., 2018) to further explore developmental relationships between human monocytes and airway macrophages in bronchiectasis. The Slingshot analysis predicted a trajectory from *GPR183*-monocytes toward the macrophage clusters (Fig. 10 F), consistent with potential differentiation of *GPR183*-monocytes into human lung macrophages. Overall, these results demonstrate that human monocytes recruited into the airways express GPR183, supporting the notion that GPR183 plays a conserved role in human monocyte-to-lung macrophage development.

Discussion

Macrophages reside in tissue-specific niches and cues from the local microenvironment shape their identity and function (Amit et al., 2016; Bain and MacDonald, 2022; Bleriot et al., 2020; Guilliams and Svedberg, 2021; Guilliams et al., 2020; Jenkins and Allen, 2021), yet little is known about the signals and receptors that govern occupation of macrophage niches in the lung. Here, we discovered GPR183 as a receptor for metabolic signals in the lung that promote the development of monocyte-derived macrophages. We propose the concept that increased niche "availability" due to resident macrophage depletion triggers GPR183 ligand production and monocyte recruitment as a physiological response to replenish lung macrophages. Accordingly, lung fibroblasts responded to local macrophage depletion by producing GPR183 ligand-synthesizing enzymes as well as other factors, such as CCL2 and M-CSF. Our results support the notion that oxysterol sensing via GPR183 guides monocytes to a niche that favors the interaction of monocytes and developing macrophages with fibroblasts. We postulate that cross talk with fibroblasts within the niche results in monocyte exposure to M-CSF, thereby stimulating the generation of transitional macrophages that differentiate into alveolar and interstitial lung macrophages.

Cell differentiation and function within tissues relies on cell localization in anatomical niches. Chemotactic signals and their receptors guide cells to specific tissue sites to support cell–cell interaction and communication. Previous work demonstrated that GPR183 positions immune cells within lymphoid structures to support adaptive immune responses and lymphoid tissue formation (Baptista et al., 2019; Ceglia et al., 2023; Emgård et al., 2018; Frascoli et al., 2023; Gatto et al., 2009; Li et al., 2016; Pereira et al., 2009). In addition, GPR183 supports immune cell homeostasis by providing access to cytokines (Gatto et al., 2013; Yi and Cyster, 2013). Furthermore, GPR183 promotes inflammatory responses in the intestine (Emgård et al., 2018) and the lung (Jia et al., 2018). GPR183-mediated cell recruitment also contributes to host defense against bacterial infection in the lung (Bartlett et al., 2020; Bohrer et al., 2022; Ngo et al., 2022). Finally, GPR183 has been reported to regulate macrophage infiltration and pro-inflammatory cytokine production during

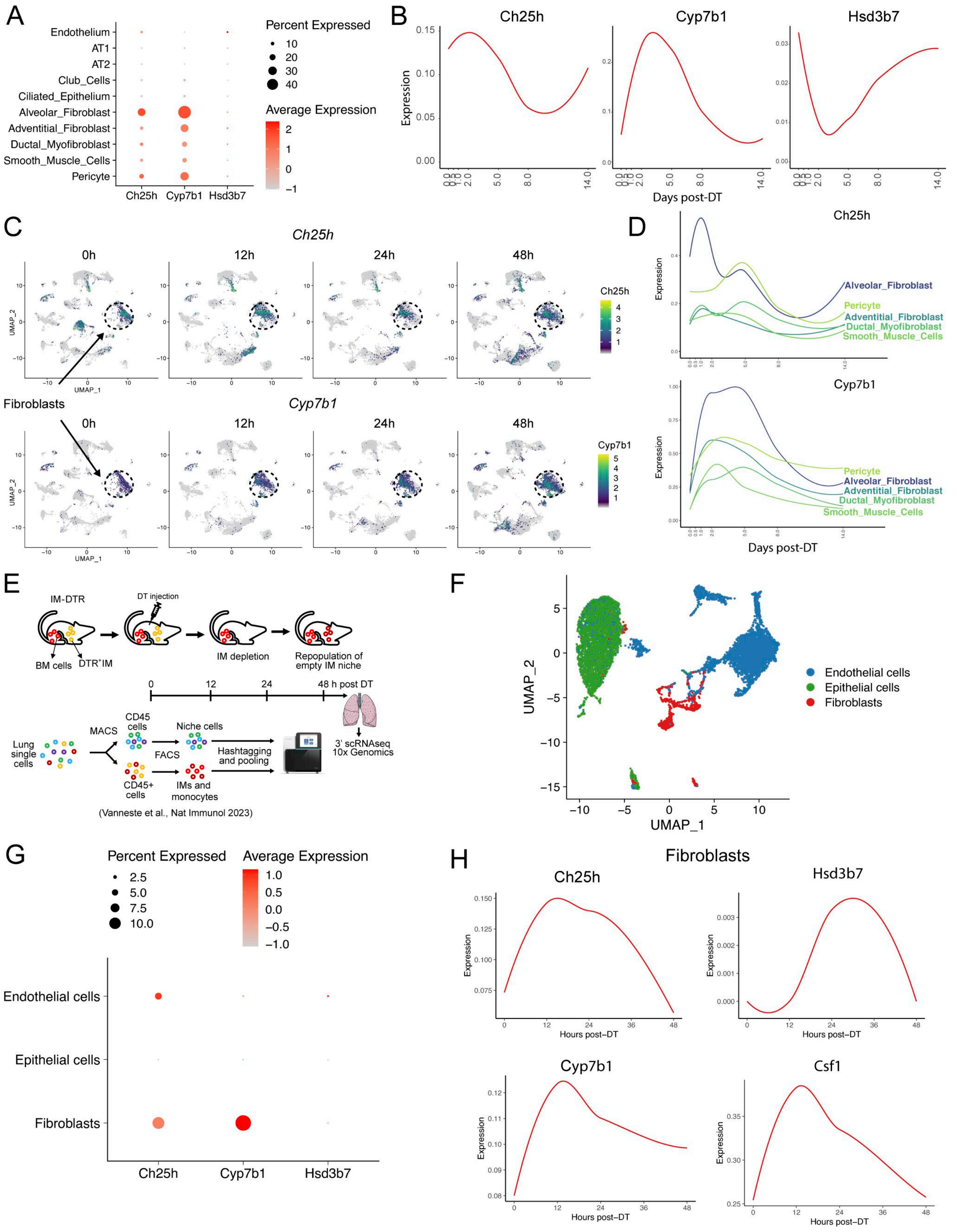

Figure 8. **Fibroblasts are the main source of GPR183 ligand-producing enzymes in the lung. (A)** Dot plot showing expression of *Ch25h*, *Cyp7b1*, and *Hsd3b7* in the indicated non-hematopoietic single-cell RNA-sequencing clusters from SPAM deleter mice as in Fig. 3 E. AT1, alveolar type I cells; AT2, alveolar type II cells. See Fig. S2 C for markers used to annotate the cell clusters. **(B)** Time course of *Ch25h*, *Cyp7b1*, and *Hsd3b7* expression in the lung of SPAM deleter mice after

DT-induced alveolar macrophage depletion as determined by single-cell RNA sequencing. **(C)** Feature plots showing *Ch25h* and *Cyp7b1* expression in the SPAM deleter cell clusters from Fig. 3 E. **(D)** Time course of *Ch25h* and *Cyp7b1* expression in the indicated SPAM deleter cell populations corresponding to the lung clusters in Fig. 3 E. Data in panels A–D are from one single-cell RNA-sequencing experiment with *n* = 4 mice per time point. **(E)** Experimental setup for single-cell RNA sequencing of lung niche cells from IM-DTR mice. CD45$^-$ non-hematopoietic cells (fibroblasts, epithelial cells, and endothelial cells) were purified from the lungs of IM-DTR mice as described in the Materials and methods. IM, interstitial macrophage. **(F)** UMAP of lung niche cells at the indicated time points after interstitial lung macrophage depletion with 50 ng intraperitoneal DT. Markers used to annotate lung fibroblasts, epithelial cells, and endothelial cells are shown in Fig. S5 A. **(G)** Dot plot of *Ch25h*, *Cyp7b1*, and *Hsd3b7* expression in lung fibroblasts, epithelial cells, and endothelial cells from IM-DTR mice. **(H)** Time course of *Ch25h*, *Cyp7b1*, and *Hsd3b7* expression in lung fibroblasts after DT-induced interstitial macrophage depletion. Data in panels F–H are from one single-cell RNA-sequencing experiment with *n* = 3–4 mice per time point. Panel E was adapted from Servier Medical Art.

SARS-CoV-2 infection in mice (Foo et al., 2023). Here, we demonstrate that oxysterol sensing via GPR183 allows monocytes to detect tissue-derived signals and occupy macrophage niches in the lung. Our findings, therefore, provide a mechanism of how monocytes sense niche availability in the lung and how they differentiate into distinct types of lung macrophages.

We discovered that GPR183 was differentially expressed in macrophages according to their location within the lung: Interstitial macrophages expressed GPR183, whereas GPR183 was absent in alveolar macrophages in the homeostatic lung. In response to macrophage depletion, alveolar macrophages derived from bone marrow monocytes transiently expressed GPR183 while establishing residence in the alveolar niche. Bone marrow monocyte–derived alveolar macrophages downregulated GPR183 expression once the lung returned to homeostasis. This raises the possibility that factors present in the homeostatic alveolar environment cause GPR183 downregulation in macrophages, whereas the interstitial niche supports GPR183 expression. We speculate that the residence time of macrophages in the alveolar niche and the status of the alveolar niche (homeostatic versus inflamed, full versus empty) may control GPR183 expression. Finally, GPR183 downregulation may be a mechanism to ensure lung homeostasis by preventing resident alveolar macrophages from responding to oxysterols.

The requirement of GPR183 for the generation of monocyte-derived lung macrophages was revealed in a competitive setting. The role of receptors, such as GPR183, in regulating cell localization *in vivo* is best studied in a competitive context because otherwise compensatory mechanisms may mask the phenotype. In the absence of cell–cell competition, cells lacking a specific chemotactic receptor can eventually access specific sites within tissues through random migration independently of chemotactic gradients. Furthermore, even if only a few receptor-deficient cells reach a specific location, these cells can replenish the niche through increased proliferation as has been shown for Kupffer cell repopulation by monocytes (Bonnardel et al., 2019). Finally, redundant chemoattractant signals and their receptors can disguise the phenotype in cells lacking a single chemotactic receptor. This phenomenon has been shown for GPR183 and CCR6 in the context of lymphoid tissue-inducer cell positioning in the intestine (Howley et al., 2023, *Preprint*). It is therefore possible that GPR183 operates in synergy with CCR2 to direct monocytes to macrophage niches in the lung.

Lack of GPR183 caused a defect in both alveolar and interstitial lung macrophages derived from bone marrow monocytes. These data indicate that GPR183 acts before monocytes make a fate decision, i.e., before they become anatomically distinct lineages of lung macrophages. Consistent with this notion, the generation of transitional monocyte-derived macrophages was dependent on GPR183. Specifically, GPR183 was required from the stage when monocytes upregulate CD64 and downregulate Ly6C surface expression. These observations suggest that GPR183 regulates the development of CD64$^+$Ly6C$^+$ monocyte-macrophage intermediates that are dependent on CCR2 and M-CSF, but independent of GM-CSF (Ruscitti et al., 2024; Vanneste et al., 2023). Overall, our findings are consistent with the notion that oxysterol sensing via GPR183 controls the fate of recruited monocytes in the lung.

It is poorly understood how monocytes occupy macrophage niches once they have entered an organ, such as the lung. The lung has a unique anatomy with a narrow interstitial space between the alveoli and the blood vessels to facilitate the gas exchange. Furthermore, the alveoli represent a special macrophage niche as only ∼30% of the alveoli are occupied by macrophages (Neupane et al., 2020). In steady state, lung monocytes reside at the interface of blood vessels and alveoli, either in the perivascular region or within capillaries in the alveolar interstitium (Rodero et al., 2015). In the current study, we found that monocytes migrated toward the GPR183 ligand 7α,25-dihydroxycholesterol *in vitro* and that recruited GPR183$^+$ monocytes *in vivo* were positioned in the proximity of *Ch25h*$^+$ lung fibroblasts that likely provide 7α,25-dihydroxycholesterol.

Cholesterol is abundant in the lung, and we demonstrate that the oxysterol 7α,25-dihdroxycholesterol functions as a migratory cue for monocytes. We found that a non-hematopoietic source of the GPR183 ligand 7α,25-dihydroxycholesterol supports monocyte-to-lung macrophage differentiation. Furthermore, we show that lung fibroblasts produce the 7α,25-dihydroxycholesterol–synthesizing enzymes CH25H and CYP7B1 in response to the loss of resident lung macrophages. Therefore, fibroblasts are likely the main cellular source of 7α,25-dihydroxycholesterol in the lung, similar to what has been reported in lymphoid organs (Yi et al., 2012) and the intestine (Emgård et al., 2018). In support of this idea, we found that *Gpr183*$^+$ monocytes/macrophages and *Ch25h*$^+$ fibroblasts co-localized in the lung. Lung endothelial cells express CH25H (Madenspacher et al., 2023) but lack CYP7B1. It is therefore possible that CH25H$^+$CYP7B1$^+$ fibroblasts and CH25H$^+$CYP7B1$^-$ endothelial cells cooperate to produce 25-hydroxycholesterol that is then further metabolized into the GPR183 ligand 7α,25-dihydroxycholesterol by fibroblast-derived CYP7B1.

Depletion of resident lung macrophages in the SPAM deleter and IM-DTR models was sufficient to increase the GPR183 ligand 7α,25-dihydroxycholesterol as well as M-CSF and CCL2, two

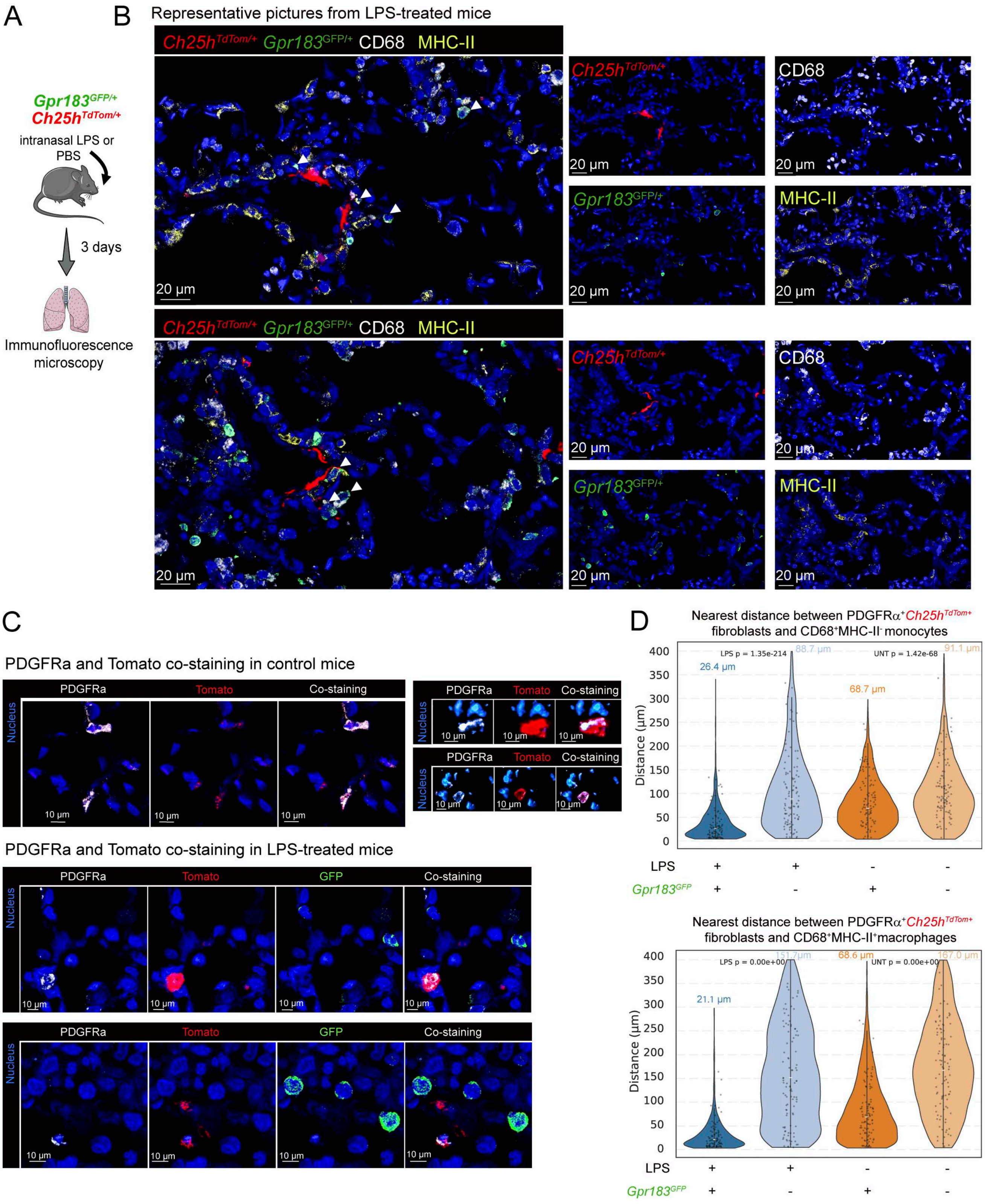

Figure 9. **GPR183-expressing monocytes interact with *Ch25h*⁺ lung fibroblasts. (A)** Experimental setup for immunofluorescence microscopy of *Gpr183*$^{GFP/+}$*Ch25h*^{tdTom} double reporter mice after intranasal LPS administration. Control mice received intranasal PBS. Lungs were harvested 3 days after LPS or PBS administration. **(B)** Representative microscopy images of lungs from LPS-treated *Gpr183*$^{GFP/+}$*Ch25h*^{tdTom} double reporter mice. Scale bars are 20 µm. Arrows indicate *Gpr183*-GFP$^+$ CD68$^+$MHCII$^-$ monocytes and CD68$^+$MHCII$^+$ macrophages located near *Ch25h*-tdTomato$^+$ cells. **(C)** Images showing co-staining of PDGFRα and tdTomato in lung fibroblasts. Scale bars are 10 µm. **(D)** Nearest distance between the indicated lung cell populations from *Gpr183*$^{GFP/+}$*Ch25h*^{tdTom} double reporter mice. Average distances and P values (by two-sided Mann–Whitney test) are shown at the top of each violin plot. Data in panels B–D are representative of two independent experiments with a total of *n* = 3 mice analyzed per group. Panel A was adapted from Servier Medical Art.

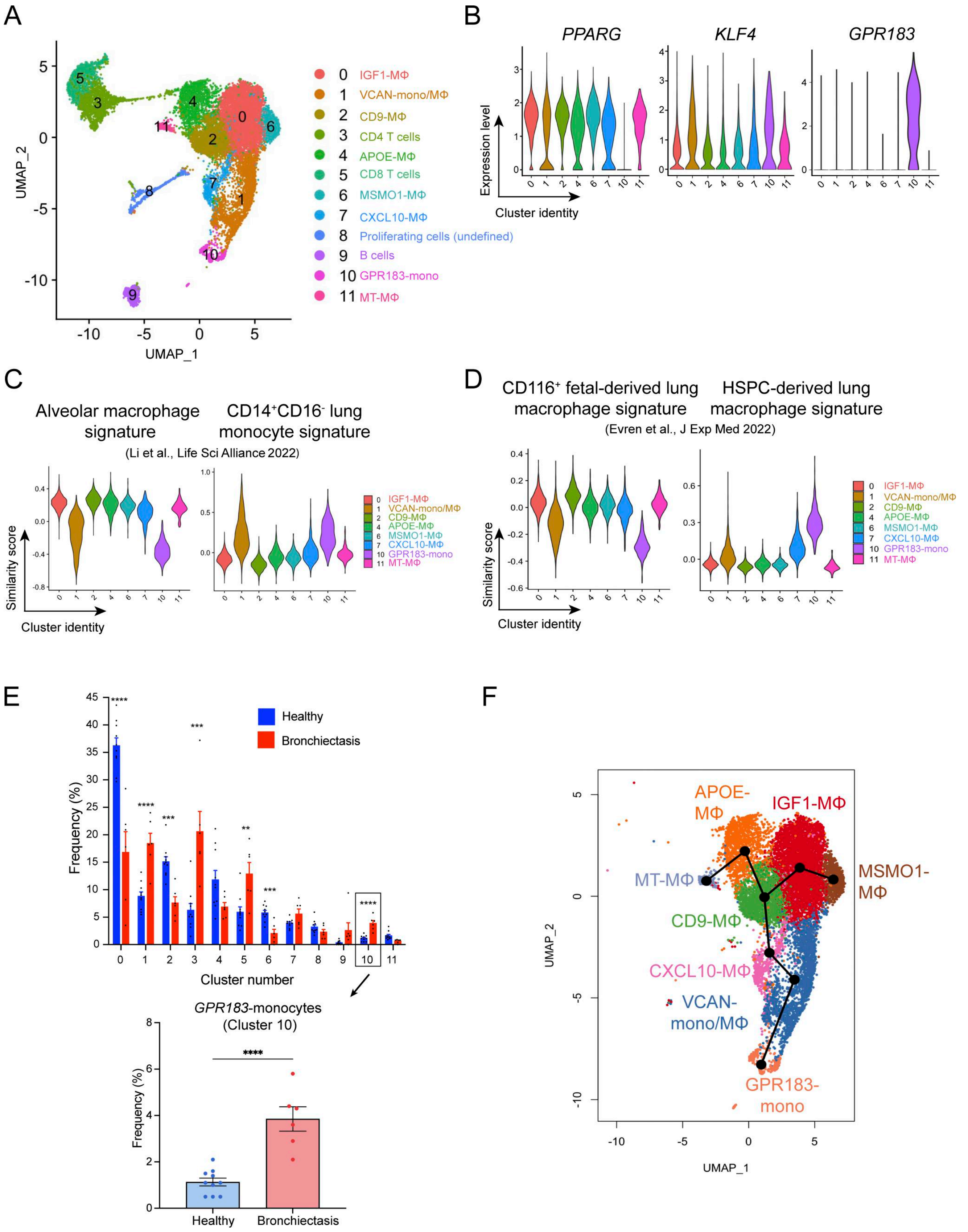

Figure 10. **Single-cell RNA sequencing identifies *GPR183*-expressing monocytes in human airway disease. (A)** UMAP showing the indicated lymphoid and myeloid cell clusters (14,437 cells) in BAL fluid after integrating single-cell RNA-sequencing datasets from six bronchiectasis patients (this study) and 10 healthy donors (Mould et al., 2021) as described in the Materials and methods. MΦ, macrophage; mono, monocyte. **(B)** Violin plots showing the expression of

the indicated genes in the myeloid clusters from panel A. **(C)** Alveolar macrophage and CD14$^+$CD16$^-$ lung monocyte signature (Li et al., 2022b) scores in the myeloid clusters from panel A. **(D)** Signature scores of human lung macrophages either derived from CD116$^+$ fetal precursors or from CD34$^+$ HSPCs (Evren et al., 2022) in the myeloid clusters from panel A. **(E)** Relative contribution of healthy (n = 10) versus bronchiectasis (n = 6) donors to each cluster in the BAL fluid. Data are represented as mean ± SEM. **P < 0.01; ***P < 0.001; ****P < 0.0001 by unpaired Student's t test. **(F)** Lineage inference analysis with slingshot of the myeloid clusters from panel A. Data in panels A–F are from one single-cell RNA-sequencing experiment with n = 6 human bronchiectasis donors that was integrated with the dataset of n = 10 healthy human donors by Mould et al. (2021).

factors required for the development of interstitial and alveolar macrophages from monocytes (Joshi et al., 2020; Sabatel et al., 2017; Schlitzer et al., 2013; Vanneste et al., 2023). This raises the possibility that the loss of resident macrophages is sensed by lung fibroblasts, which stimulates fibroblasts to produce factors that replenish the depleted niche. Consistent with this notion, recent work demonstrated that sensing of physical space and cell density by fibroblasts controls macrophage number within the niche through M-CSF production (Zhou et al., 2022). Coordinated upregulation of *Ch25h*, *Cyp7b1*, *Ccl2*, and *Csf1* after depletion of resident macrophages supports the concept that fibroblasts act as a hub that not only provides growth factors, such as M-CSF, according to the two-cell circuit proposed by Medzhitov (Zhou et al., 2018), but also a cholesterol metabolite to position monocytes and to support macrophage differentiation.

In conclusion, our study provides mechanistic insights into how metabolic signals recognized by GPR183 direct the migration of monocytes and instruct their differentiation into distinct types of lung macrophages. This knowledge is relevant to the aim of reprogramming macrophages to improve the outcome of lung disease in humans. Targeting GPR183 and cholesterol metabolism could be a new way to limit lung pathology, especially because GPCRs are excellent drug targets.

Limitations of the study

GPR183 was dispensable for the development of resident macrophages in the steady-state lung. However, it is possible that GPR183 supports the development of embryonic-derived lung macrophages in a competitive setting. In the current study, we used genetic and genotoxic models of macrophage depletion to investigate the role of GPR183 in monocyte-derived lung macrophages. It will be worthwhile extending our findings in future studies using more physiologically relevant contexts, such as after lung infection. In addition, a cell type–specific genetic loss of oxysterol enzymes would be required to directly demonstrate that GPR183 ligand produced by fibroblasts promotes the development of monocyte-derived lung macrophages.

Materials and methods

Mice

Gpr183$^{-/-}$ and *Gpr183*$^{\mathrm{GFP}/+}$ mice were previously described (Emgård et al., 2018; Pereira et al., 2009). *Ch25h*$^{-/-}$ mice were obtained from The Jackson Laboratory (strain #016263). *Ch25h*$^{\mathrm{tdTom}}$ mice (Frascoli et al., 2023) were crossed with *Gpr183*$^{\mathrm{GFP}/+}$ mice to generate *Gpr183*$^{\mathrm{GFP}/+}$*Ch25h*$^{\mathrm{tdTom}}$ double reporter mice. IM-DTR (*Tmem119*$^{\mathrm{Cre}}$ *Cx3cr1*$^{\mathrm{LSL\text{-}DTR}}$) mice to deplete interstitial lung macrophages were described by Vanneste et al. (2023). SPAM deleter (*Epx*$^{\mathrm{Cre}}$ *Siglecf*$^{\mathrm{Lox\text{-}DTR\text{-}Lox}}$) mice to deplete alveolar macrophages were described by Verwaerde et al. (2025). C57BL/6 (B6) CD45.1$^+$ (B6.SJL-*Ptprc*^{a}*Pepc*^{b}/BoyJ) mice were obtained from in-house breeding. Both male and female mice at least 6 wk old were used for experiments with similar results. Co-housed *Gpr183*$^{+/+}$ littermates were used as controls for experiments with *Gpr183*$^{-/-}$ mice. All mouse strains were housed in individually ventilated cages in specific pathogen-free conditions. Animal experiments were approved by the Linköping Ethics Committee (#20547-2021), the Animal Care and Use Committee of the University of Liège, Liège, Belgium (#2642), the Animal Ethics Committee of Ghent University (#LA1400091/LA2400526), as well as the Animal Care and Use Committee of UMass Chan Medical School (#202000151, 201900263) and performed in accordance with institutional guidelines.

Human tissue samples

BAL fluid was collected from patients with bronchiectasis at Karolinska University Hospital Huddinge, Huddinge, Sweden, by bronchoscopy. See Table S1 for information on bronchiectasis patients. The Swedish Ethical Review Authority approved the collection of human BAL fluid (#2019-00618, 2020-07094). Informed consent was obtained from all donors after giving verbal and written information.

Bone marrow chimeras

In general, to generate bone marrow chimeras, recipient mice underwent whole-body irradiation with 2 × 5 Gy before receiving 2 × 10^6 bone marrow cells by tail vein injection. Irradiated mice were kept on antibiotic prophylaxis (Sulfatrim) in drinking water for 3 wk. To determine *Gpr183* mRNA expression in monocyte-derived alveolar macrophages, irradiated B6 mice (CD45.1$^+$) were injected with bone marrow from either *Gpr183*$^{\mathrm{GFP}/+}$ or *Gpr183*$^{\mathrm{GFP/GFP}}$ reporter mice (CD45.2$^+$) and analyzed 3, 5, and 12 wk after bone marrow injection (Fig. 2, E and F). Irradiated B6 mice (CD45.1$^+$) injected with bone marrow from either *Gpr183*$^{+/+}$ or *Gpr183*$^{+/-}$ mice (CD45.2$^+$) were used as controls. For competitive bone marrow chimeras, irradiated B6 CD45.1$^+$ recipient mice were injected with a 1:1 mixture of *Gpr183*$^{+/+}$ (CD45.1.2$^+$) and *Gpr183*$^{-/-}$ (CD45.2$^+$) or *Gpr183*$^{+/+}$ (CD45.2$^+$) and *Gpr183*$^{-/-}$ (CD45.1.2$^+$) bone marrow cells. Competitive bone marrow chimeras were analyzed at 3 wk (Fig. 7, A and B), 9–13 wk (Fig. 4, A and B), 19–23 wk (Fig. 4 C), or 9–29 wk (Fig. 4 E) after bone marrow transfer. Single-transfer bone marrow chimeras (Fig. 4 D) were generated by injecting irradiated B6 mice (CD45.1$^+$) with either *Gpr183*$^{+/+}$ or *Gpr183*$^{-/-}$ bone marrow cells (CD45.2$^+$) and analyzed 7–8 wk after bone marrow transfer. Mixed *Gpr183*$^{+/+}$/*Rag1*$^{-/-}$ and *Gpr183*$^{-/-}$/*Rag1*$^{-/-}$ chimeras (Fig. 6, A and B) were generated by injecting irradiated B6 mice (CD45.1$^+$) with a 1:1 mixture of either *Gpr183*$^{+/+}$ (CD45.1.2$^+$) and

Rag1$^{-/-}$ (CD45.2^{+}) bone marrow or *Gpr183*$^{+/+}$ (CD45.1.2^{+}) and *Rag1*$^{-/-}$ (CD45.2^{+}) bone marrow. Analysis of chimeras was performed at 10 wk after bone marrow transfer. Mixed *Gpr183*$^{+/+}$/*Ccr2*$^{RFP/RFP}$ and *Gpr183*$^{-/-}$/*Ccr2*$^{RFP/RFP}$ chimeras were generated in an analogous manner and analyzed 9–10 wk after bone marrow injection (Fig. 6, C and D). To determine the role of 7α,25-dihydroxycholesterol in monocyte-to-lung macrophage differentiation, irradiated *Ch25h*$^{-/-}$ mice or *Ch25h*$^{+/+}$ controls (CD45.2^{+}) were reconstituted with an equal mixture of *Gpr183*$^{+/+}$ (CD45.1.2^{+}) and B6 (CD45.1^{+}) or *Gpr183*$^{-/-}$ (CD45.1.2^{+}) and B6 (CD45.1^{+}) bone marrow cells (Fig. 7 C). Chimeras were analyzed 7–15 wk after bone marrow transfer. To distinguish a hematopoietic versus a non-hematopoietic source of *Ch25h*, irradiated *Ch25h*$^{+/+}$ or *Ch25h*$^{-/-}$ mice were reconstituted with either *Ch25h*$^{+/+}$ or *Ch25h*$^{-/-}$ bone marrow cells as indicated (Fig. 7 D). Lungs were harvested 3–4 wk after bone marrow transfer for quantitative RT-PCR to determine *Ch25h* mRNA expression.

Alveolar and interstitial lung macrophage depletion

To deplete alveolar macrophages, *Epx*^{Cre} *Siglecf*$^{Lox\text{-}DTR\text{-}Lox}$ mice, named "SPAM deleter" mice (Verwaerde et al., 2025), were used (Fig. 3 A). In *Siglecf*$^{Lox\text{-}DTR\text{-}Lox}$ mice, DTR is expressed in alveolar macrophages and eosinophils. To confer alveolar macrophage–specific DTR expression, *Siglecf*$^{Lox\text{-}DTR\text{-}Lox}$ mice were crossed with *Epx*^{Cre} mice, which results in excision of DTR in eosinophils as they express eosinophil peroxidase (Epx). In *Epx*^{Cre} *Siglecf*$^{Lox\text{-}DTR\text{-}Lox}$ mice, DTR is only expressed in alveolar macrophages, thereby allowing their specific depletion after DT administration (Fig. 3, B and C). For depletion of alveolar macrophages, SPAM deleter mice received the following concentrations of intratracheal DT: 100 pg for flow cytometry (Fig. 3, B and C) and cytokines/chemokines in BAL fluid (Fig. S2, A and B), 1 ng for bone marrow chimeras (Fig. 5, A and B), and 40 ng for the single-cell RNA-sequencing experiment (Fig. 3, E–G; Fig. 8, A–D; Fig. S2, C–E; and Fig. S5, B and C). To generate SPAM deleter bone marrow chimeras, SPAM deleter mice (CD45.2^{+}) were preconditioned by busulfan administration (30 mg/kg body weight by intraperitoneal injection) to preserve resident alveolar macrophages. Preconditioned SPAM deleter mice (CD45.2^{+}) were then injected intravenously with a 1:1 mixture of 3 × 10^{6} *Gpr183*$^{+/+}$ or *Gpr183*$^{-/-}$ (CD45.1.2^{+}) and B6 (CD45.1^{+}) bone marrow cells (Fig. 5 A). 7 wk after bone marrow transfer, resident alveolar macrophages (CD45.2^{+}) were depleted by intratracheal administration of 1 ng DT. 4 wk after DT administration, reconstitution of the alveolar macrophage compartment was assessed by flow cytometry. For depletion of interstitial lung macrophages, we used IM-DTR (*Tmem119*^{Cre} *Cx3cr1*$^{LSL\text{-}DTR}$) mice (Vanneste et al., 2023). To generate IM-DTR bone marrow chimeras, IM-DTR mice (CD45.1.2^{+}) were preconditioned by thorax-shielded irradiation with two doses of 6 Gy using a 0.6-cm-thick lead cover to preserve resident interstitial lung macrophages as described (Vanneste et al., 2023). After irradiation, mice received 0.05 mg/ml of enrofloxacin (Baytril, Bayer) in drinking water for 4 wk. After preconditioning, IM-DTR mice (CD45.1.2^{+}) were injected intravenously with a 1:1 mixture of 10 × 10^{6} *Gpr183*$^{+/+}$ or *Gpr183*$^{-/-}$ (CD45.2^{+}) and B6 (CD45.1^{+}) bone marrow cells (Fig. 5 C). 4 wk after bone marrow transfer, resident interstitial lung macrophages (CD45.2^{+}) were depleted by a single intraperitoneal injection of 50 ng DT (List Biological Labs) as described (Vanneste et al., 2023). 2 wk after DT injection, repopulation of the interstitial lung macrophage compartment was examined by flow cytometry.

Cell isolation from mice

BAL fluid was obtained by inserting a catheter into the trachea and flushing with 5 × 1 ml warm buffer (0.5% FCS/2 mM EDTA/PBS). After collecting BAL fluid, lungs were harvested. For flow cytometry, harvested non-perfused lungs were digested in RPMI 1640/5% FCS with 0.2 mg/ml of collagenase IV (Sigma-Aldrich) and 0.02 mg/ml of DNase I (Sigma-Aldrich) for 60 min at 37°C, and immune cells were purified as previously described (Evren et al., 2021). Blood obtained by cardiac puncture was diluted in 200 U/ml heparin (Sigma-Aldrich), and red blood cell lysis was performed before staining cells for flow cytometry. Bone marrow cells were isolated from femur and tibia by flushing with RPMI 1640/10% FCS/1% L-glutamine/penicillin/streptomycin/55 mM 2-mercaptoethanol before red blood cell lysis. Spleen cells were obtained by cutting the spleen into small pieces, followed by digestion for 30 min as described above for lungs (but without density gradient centrifugation). Cells from the peritoneal cavity were obtained by lavage as described (Ray and Dittel, 2010). Liver cells were isolated using protocols by either Kong et al. (2024) or Daemen et al. (2021). Brains were dissected, cut into small pieces with a scalpel and enzymatically digested using Neural Tissue Dissociation Kit T (Miltenyi Biotec) for 30 min at 37°C. Myelin was removed using 38% Percoll (Sigma-Aldrich), and red blood cells were lysed using ACK lysis buffer (Thermo Fisher Scientific).

Flow cytometry

Single-cell suspensions from various organs were first stained in FACS buffer (PBS/2% FCS) for 30 min on ice with fluorochrome- or biotin-labeled antibodies (Table S2). Then, secondary staining with streptavidin–Brilliant Violet 711 or streptavidin–BUV395 (BD Biosciences) was performed for 30 min on ice. All antibodies were pre-titrated to minimize nonspecific staining. After surface staining, cells were stained with fixable viability dye eFluor 506 (Thermo Fisher Scientific) and then fixed in PBS/2% paraformaldehyde before acquisition on a LSR II Fortessa or Symphony A5 flow cytometer (BD Biosciences). Data were analyzed with FlowJo version 10 software (https://www.flowjo.com/solutions/flowjo/downloads).

Quantification of proteins in BAL fluid

Cytokines and chemokines in the BAL fluid from SPAM deleter mice were quantified by ELISA using kits from Thermo Fisher Scientific and R&D Systems following the manufacturer's instructions.

Chemotaxis assays

Ly6C^{hi} monocytes were enriched from bone marrow by immunomagnetic selection with the Monocyte Isolation kit (Miltenyi Biotec) according to the manufacturer's instructions. After isolation, monocytes were resensitized in migration medium

(RPMI 1640/0.5% fatty acid–free BSA/10 mM HEPES) for 30 min at 37°C/5% CO_2. Then, monocyte migration toward the indicated concentrations of 7α,25-dihydroxycholesterol (Merck) was determined using 5 µM Transwells (Corning). Monocytes (0.5–1 × 10^5 cells per well) were allowed to migrate for 3 h. Cells in the bottom chamber were harvested and mixed with CountBright Absolute Counting Beads (Thermo Fisher Scientific) for quantification of migrated cells by flow cytometry. The frequency of cells compared with input was used to define the chemotactic response to 7α,25-dihydroxycholesterol.

In vitro macrophage differentiation

Bone marrow cells were isolated from the indicated mouse strains. Cells (5–10 × 10^5 per well) were then cultured in 12-well plates containing medium (DMEM/10% FCS/1% L-glutamine/penicillin/streptomycin) supplemented with either 20 ng/ml M-CSF (Thermo Fisher Scientific) to generate generic macrophages or 20 ng/ml GM-CSF and 2 ng/ml TGFβ_1 (Thermo Fisher Scientific) to generate alveolar macrophage–like cells (Luo et al., 2021). Medium was refreshed on day 7. On day 9, cells were harvested using 0.05% trypsin-EDTA and a cell scraper and stained for flow cytometry as described above.

Alveolar macrophage metabolism

To determine the single-cell metabolism of alveolar macrophages, the SCENITH (Arguello et al., 2020) method was used. Briefly, BAL fluid was harvested from competitive *Gpr183*$^{+/+}$/*Gpr183*$^{-/-}$ bone marrow chimeras in homeostatic conditions, i.e., 9–11 wk after bone marrow transfer. BAL cells from two to three mice were pooled and then seeded in 96-well V-bottom plates in 100 µl medium (RPMI 1640/10% FCS/1% pyruvate/GlutaMAX/penicillin/streptomycin) at 5 × 10^4 cells per well. In the first out of two independent experiments, a sufficient number of cells allowed for technical duplicates. Cells were then incubated for 30 min at 37°C/5% CO_2 with various metabolic inhibitors as described (Arguello et al., 2020). Next, cells were incubated with 10 µM puromycin (Sigma-Aldrich) for another 30 min at 37°C/5% CO_2 and harvested. After surface staining, cells were fixed and permeabilized with the FoxP3/Transcription Factor Staining Buffer Set (Thermo Fisher Scientific) before intracellular staining with a 1:400 dilution of anti-puromycin-PE antibody (clone 2A4; BioLegend) at 4°C overnight. After flow cytometry, metabolic values were calculated as described (Arguello et al., 2020).

Quantitative RT-PCT

Accessory lobes of the lungs were homogenized in TRIzol reagent (Invitrogen) using a tissue homogenizer (PT 2500 E; Polytron) and total RNA extracted according to the manufacturer's instructions. cDNA was synthesized from 1.6 to 2.0 µg of total RNA with the SuperScript First-Strand Synthesis System (Invitrogen). cDNA and primer-probe sets from either Applied Biosystems (*Ch25h*) or Sigma-Aldrich (*Hprt*) were used for quantitative RT-PCR on a QuantStudio 5 Real-Time PCR system (Applied Biosystems).

Single-cell RNA sequencing of human BAL cells

For single-cell RNA sequencing, frozen BAL samples from six patients with bronchiectasis were used (Table S1). As samples were collected sequentially from different patients, they were frozen to be able to process all samples together for library preparation (see below). BAL fluid from bronchiectasis patients was centrifuged and the pellet resuspended in RPMI 1640/5% FCS before freezing. Frozen BAL samples were thawed, treated with 50 U/ml Benzonase Endonuclease (Merck) for 20 min at 37°C, and then live CD45$^+$CD66$^-$ cells were purified by cell sorting. Neutrophils (CD66$^+$) were excluded as they are prone to cell death, especially after thawing. Single-cell libraries from purified cells were prepared with the 10x Genomics Single Cell NEXT GEM 3′ Library version 3 kit according to the manufacturer's instructions. Libraries were then sequenced on a NextSeq 2000 (Illumina) and mapped to the human genome (GRCh37) with the Cell Ranger 3.0.2 pipeline from 10x Genomics. The R software package Seurat 4.1.1 was used for analysis. To compare the distribution of airway macrophages and monocytes in health and disease, we integrated our bronchiectasis dataset with the healthy BAL dataset by Mould et al. (2021). For this purpose, the 10 healthy control samples by Mould et al. (2021) were merged into one Seurat object and the Seurat object downsampled to 10,000 total cells. Then, the downsampled object was merged with our six bronchiectasis samples. Next, low-quality cells and doublets were removed based on the following criteria: (1) <200 and >6,000 unique genes expressed in at least three cells, (2) >20% mitochondrial content, and (3) < 5% ribosomal content. The FindVariableFeatures function was applied to select 2,000 highly variable genes, followed by ScaleData to produce a principal component analysis and neighborhood graph with 50 principal components. Then, all cells were integrated using the FindIntegrationAnchors function in Seurat, and dimensionality reduction was applied to the integrated space. Louvain clustering was performed with the FindClusters function set to 0.8, resulting in 11 clusters with 14,437 cells (Fig. 10 A). Wilcoxon rank-sum test with logfc. threshold = 0.2 as well as min.pct = 0.1 and min.diff.pct = 0.2 was employed to identify cluster-specific differentially expressed genes. Clusters were assigned cell type identities based on the expression of known cell type–specific marker genes. The lymphoid clusters were then removed by creating a new Seurat object of only myeloid clusters (clusters 0, 1, 2, 4, 6, 7, 10, and 11) with 10,978 cells. The expression of selected genes was visualized in the cell clusters with the ViolinPlot function in Seurat. The GeneModuleScore function in Seurat was used to assess the similarity of the bronchiectasis cell clusters to human monocyte and macrophage populations in terms of their gene signatures. The following published single-cell RNA-sequencing datasets were used for the gene signature score analysis: Alveolar macrophages and CD14$^+$CD16$^-$ monocytes from human lung (Li et al., 2022b), as well as human lung macrophages either derived from CD116$^+$ fetal precursors or from CD34$^+$ HSPCs in MISTRG mice (Evren et al., 2022). To infer lineage trajectories between the monocyte and macrophage clusters in bronchiectasis, the R package Slingshot 2.4.0 (https://www.bioconductor.org/packages/release/bioc/html/slingshot.html) was used. The analysis was done in an unsupervised fashion, without defining any cluster as starting point or endpoint.

Single-cell RNA sequencing of lung cells from SPAM deleter mice

Lungs were harvested from SPAM deleter mice 0, 12, 24, and 48 h and on day 5, 8, and 14 after alveolar macrophage depletion with 40 ng DT intratracheally (Fig. 3 D). Four mice (two males and two females) were used per time point. $CD45^-$ nonhematopoietic cells (50% of lung cells) as well as resident $CD45^+CD64^+$ (25% of lung cells) and $CD45^+CD64^-$ hematopoietic cells (25% of lung cells) were isolated by cell sorting. Lung-resident cells were identified as cells that were protected from intravascular labeling with 1 µg intravenously injected anti-mouse CD45 antibody (clone 30-F11). After cell isolation, up to 2×10^6 cells per mouse were centrifuged (400 *g*, 5 min, 4°C) and then resuspended in 50 µl of staining mix in PBS containing 0.04% PBS, TruStain FcX Block (BioLegend), fluorescent surface antibodies, and mouse CITE-Seq antibody panel, a unique mouse TotalSeq-C cell hashing antibody (BioLegend) diluted 1:1,000. The CITE-Seq panel (Table S3) contains 192 unique oligo-conjugated antibodies and isotype controls (BioLegend, TotalSeq-C). Replicates were tagged and pooled using TotalSeq-C hashtag antibodies specific against mouse CD45 and MHC class I (BioLegend; TotalSeq-C0301, TotalSeq-C0302, TotalSeq-C0303, and TotalSeq-C0304). TotalSeq-C hashtag oligonucleotides (HTOs) were used to distinguish the origin of cell from different mice. After 30-min incubation on ice, cells were washed (400 g, 5 min, 4°C) and resuspended in PBS/0.04% BSA. Cells were sorted from single-cell suspensions using a FACS Aria II/III (BD Biosciences). Sorted single-cell suspensions were resuspended at an estimated final concentration of 1,200–2,000 cells/µl and loaded on a Chromium GemCode Single Cell Instrument (10x Genomics) to generate single-cell Gel beads-in-EMulsion. The DNA libraries were prepared using the GemCode Single Cell 5′ Gel Bead and Library kit, version Next GEM version 2 according to the manufacturer's instructions (10x Genomics, User Guide CG000330). Size selection with SPRIselect Reagent Kit (Beckman Coulter) was used to separately amplify cDNA molecules for 5′ gene expression and cell surface protein construction. The cDNA content of pre-fragmentation and postsample index PCR samples was analyzed using the 2100 Bioanalyzer (Agilent). Sequencing libraries were loaded on an Illumina NovaSeq flow cell at VIB Nucleomics Core on the Illumina NovaSeq 6000 platform with a read configuration of 28 cycles for read 1, 10 cycles for i7 index, 10 cycles for i5 index, and 90 cycles for read 2, incorporating 1% PhiX as a sequencing control, pooled in an 90:10 ratio for the combined 5′ gene expression and cell surface protein samples, respectively. The Cell Ranger pipeline (10x Genomics, version 6.1.1) was used to perform sample demultiplexing and to generate FASTQ files for read 1, read 2, and the i5, i7 sample index for the gene expression and cell surface protein libraries. Read 2 of the gene expression libraries was mapped to the reference mouse genome GRCm 38.99. Subsequent barcode processing, unique molecular identifiers, filtering, and gene counting were performed using the Cell Ranger suite (10x Genomics). Single-cell RNA sequencing analysis was conducted in R, beginning with the complete, unfiltered count matrix. The analysis followed the workflow described by the Marioni and Theis laboratories (Luecken and Theis, 2019). Cells expressing fewer than 200 genes and genes detected in fewer than three cells were excluded from further analysis. HTO data were incorporated using the CreateAssayObject function from the Seurat package (version 3.1.5). HTO counts were normalized using the centered log-ratio method. Demultiplexing was performed using both HTODemux and MultiSeqDemux functions from Seurat. Quality control filtering was applied to remove outliers based on three metrics: number of expressed genes, library size, and mitochondrial gene proportion. Cells exceeding five median absolute deviations from the median for the number of expressed genes or total counts were excluded. Additionally, cells with a mitochondrial gene proportion exceeding five median absolute deviations above the median were removed. This filtering strategy was applied to be lenient. Finally, for each of the samples, the Seurat (version 4.0.2) workflow was used to normalize, cluster, and visualize the gene expression data. Clustering and visualization were performed with FindNeighbors(), FindClusters(), and RunUMAP(). To demultiplex the HTO-labeled data, we used MultiSeqDemux() from Seurat with autoThresh = TRUE. Annotation was performed using differentially expressed gene sets obtained with the FindAllMarkers function. Doublets clusters were identified as concomitant expression patterns for different cell types and excluded from the analysis. This was further validated using the DoubletFinder (version 2.0). Standard visualization was done using DimPlot, FeaturePlot, and DotPlot functions from Seurat. Gene expression over time for indicated genes was smoothed using Loess regression.

Single-cell RNA sequencing of lung niche cells from IM-DTR mice

Lungs were collected from IM-DTR mice at 0, 12, 24, and 48 h following interstitial macrophage depletion induced by intraperitoneal injection of 50 ng DT, with three to four mice analyzed per time point (Fig. 8 E). Single-cell suspensions were obtained after enzymatic digestion and nonhematopoietic $CD45^-$ niche cells were isolated by MACS using CD45 MicroBeads (Miltenyi Biotec). Lung endothelial cells, epithelial cells, and fibroblasts were then FACS sorted separately as $CD45^-CD31^+EpCAM^-$, $CD45^-CD31^-EpCAM^+$ and $CD45^-CD31^-EpCAM^-$ cells, respectively. Sorted lung endothelial cells, epithelial cells, and fibroblasts were pooled at an equicellular ratio of 1:1:1. Cells were then barcoded per time point post-DT injection with TotalSeq-A anti-mouse Hashtag antibodies (BioLegend). Hashtag barcoded cells were washed, pooled, spun down, and resuspended in PBS with 0.04% UltraPure BSA (Thermo Fisher Scientific) at a final concentration of 500 cells/µl. Cell suspensions were loaded into the Chromium Controller (10x Genomics) at a target recovery of 3×10^3 cells per time point post-DT injection. Cells were encapsulated and partitioned, and their polyA RNAs were captured and barcoded using Chromium Single Cell 3′ GEM, Library & Gel Bead Kit version 3 (10x Genomics). The cDNAs were amplified and libraries compatible with Illumina sequencers were generated using Chromium Single Cell 3′ GEM, Library & Gel Bead Kit version 3 (10x Genomics). For HTO library, 1 µl HTO additive primer v2 (0.2 µM stock) were added to the mix at the cDNA amplification step. The libraries were sequenced on an Illumina NovaSeq sequencer on an SP100 cell flow (read 1, 28 cycles; read 2, 76 cycles; index i7, 10 cycles; index i5, 10 cycles) with a sequencing depth of 20,000 reads per cell. Single-cell RNA-sequencing data were processed using Cell Ranger (version 3.0.2) for demultiplexing, alignment to the mouse reference genome (GRCm38/mm10), filtering, unique molecular identifier counting, and generation of gene-barcode matrices. Downstream analysis was carried out in R (version 4.0.3) using the Seurat package (version 4.0.0). For each sample, filtered matrices containing cell barcodes and gene features were used to construct Seurat objects. Quality control included removal of cells with fewer than 200 detected genes, genes expressed in fewer than three cells, and cells with over 20% mitochondrial gene content. Gene expression was normalized using the default LogNormalize method (scale factor: 10,000), followed by log transformation. The top 2,000 highly variable genes were identified using the vst method. Clustering was performed using the FindClusters function, and cell types were annotated with the SingleR package. Contaminating immune cells were excluded from the final dataset.

Immunofluorescence microscopy

To induce local airway inflammation and monocyte recruitment, *Gpr183*$^{\text{GFP/+}}$*Ch25h*$^{\text{tdTom}}$ double reporter mice received 50 µg LPS from *Escherichia coli* O55:B5 (Sigma-Aldrich) via the intranasal route (Fig. 9 A). Control mice received the same volume of PBS. On day 3 after intranasal LPS or PBS treatment, lungs were perfused with 20 ml cold PBS and slowly inflated with 1–1.5 ml 50% Optimal Cutting Temperature compound in PBS. Harvested lung were fixed in 1.3% PFA for 6 h at 4°C. After washing three times with PBS, fixed lungs were dehydrated by incubation in a successive sucrose gradient (10% → 20% → 30% sucrose in PBS). Finally, lungs were frozen in a slurry of ethanol on dry ice, embedded in OCT, and stored at −80°C before preparing 7-µm sections. Lung sections were first stained for 2 h at room temperature in blocking buffer (0.3% Triton X-100 [Merck] and 2% donkey serum in PBS) with rat anti-mouse CD68 (1:50) and rabbit anti-mouse PDGFRα (1:50) primary antibodies. After washing sections with PBS three times, anti-rat AF647 (1:500) and anti-rabbit AF750 (1:250) secondary antibodies were added in blocking buffer and incubated for 2 h in the dark at room temperature, then washed with PBS three times. Sections were further stained with anti-GFP AF488 (1:200) and anti-tdTom DyLight 550 (1:100) for 2 h in the dark at room temperature. After washing, samples were incubated with MHC-II AF700 antibody (1:100) for 2 h in the dark at room temperature. Finally, sections were washed three times with PBS and were mounted with 10 µl Fluoromount-G reagent (Invitrogen) containing 0.3% SYTOX blue nucleic acid stain (Invitrogen) and stored at 4°C in the dark until imaging. Confocal images were acquired using a Leica Stellaris 8 Inverted Confocal Microscope equipped with a White Light Laser, using a 40×/1.30 NA oil-immersion objective. Image resolution was set at 512 × 512 pixels with unidirectional scanning at 400 Hz. Cell types within lung sections (Fig. 9, B and C) were defined as monocytes (CD68$^+$MHCII$^-$), macrophages (CD68$^+$MHCII$^+$), and fibroblasts (PDGFRα$^+$). Antibodies against GFP and tdTomato were used to visualize *Gpr183*$^+$ and *Ch25h*$^+$ cells, respectively. Microscopy images were analyzed using QuPath (version 0.5.1) (Bankhead et al., 2017). Out of focus regions and obvious artefacts were manually excluded prior to quantification. Nuclei were identified using the Sytox counterstain and segmented with the StarDist plugin (Schmidt et al., 2018, *Preprint*), applying the pretrained model dsb2018_heavy_augment.pb. QuPath measurement tables were exported and processed in Python, including nuclear centroid coordinates (X/Y, µm) and per-cell morphology and fluorescence-intensity features. Marker positivity was determined by supervised classification on a per-image basis to account for staining variability. For each marker channel (CD68, GFP, PDGFRα, MHCII, and tdTomato), a set of cells was manually annotated as positive or negative based on visual inspection, and a random forest classifier was trained using QuPath-derived features and then applied to all detected cells in the same image. Classification was performed independently for each marker, and cell populations were defined by combinatorial marker expression (monocytes: CD68$^+$MHC-II$^-$; macrophages: CD68$^+$MHC-II$^+$; PDGFRα$^+$tdTomato$^+$CD68$^-$ fibroblasts; GFP$^+$ versus GFP$^-$ subsets). The abundance of each population was quantified per image. For the double-reporter experiments (Fig. 9), three biological replicates (mice) per condition were analyzed (LPS and control), with four images in total quantified for the LPS group and three images in total for the control group. Spatial proximity between populations was quantified using nearest neighbor distances computed from nuclear centroid coordinates with scipy.spatial.distance (SciPy version 1.15.2). For a given source population, Euclidean distances to all cells in a target population were computed, and the minimum distance was recorded for each source cell; distances <1 µm were excluded to minimize artefacts due to overlapping nuclei or segmentation uncertainty. For the analysis shown in Fig. 9 D, nearest neighbor distances were computed from each PDGFRα$^+$tdTomato$^+$CD68$^-$ fibroblast to the closest CD68$^+$MHC-II$^-$ monocyte or CD68$^+$MHC-II$^+$ macrophage, such that each value contributing to the violin plots corresponds to one fibroblast. Smaller nearest neighbor distances indicate fibroblasts with a monocyte/macrophage in close proximity, whereas larger nearest neighbor distances reflect fibroblasts that are comparatively isolated from monocytes/macrophages in that field. Nearest neighbor distances were pooled across images within each experimental group and summarized as violin plots. Nearest neighbor analysis was selected because it provides an interpretable per-cell measure of local proximity that is well suited to centroid-based segmentation, avoids selecting an arbitrary neighborhood radius, and is robust to heterogeneous lung tissue geometry (airspaces and excluded regions).

Statistical analysis

Data are presented as mean and SEM in the figures. The number of biological replicates (*n*) and repeat experiments are stated in the figure legends. Statistical tests used were Student's *t*, Welch's *t*, or Mann–Whitney test (for comparison between two groups) and one-way ANOVA with post hoc testing using Tukey's multiple comparison test (for multigroup comparisons). To determine statistical significance, two-sided testing was applied with $\alpha = 0.05$. P values for statistical significance are shown in the figures. Statistical analysis was performed with GraphPad Prism 9 (https://www.graphpad.com/scientific-software/prism/).

Online supplemental material

Fig. S1 shows the flow cytometry gating strategy to identify immune cells in the mouse lung and is relevant for Figs. 1, 2, 4, 6, and 7. Fig. S2 (relevant for Fig. 3; Fig. 8, A–D; and Fig. S5, B and C) shows concentrations of cytokines and chemokines in the BAL fluid of SPAM deleter mice as well as marker genes used to delineate single-cell RNA-sequencing cell clusters in the lung of SPAM deleter mice. Fig. S3 shows the flow cytometry gating strategy to identify monocytes and macrophages in tissues other than the lung in Fig. 4 E. Fig. S4 (relevant for Fig. 4) shows the energy metabolism of alveolar macrophages isolated from competitive *Gpr183*$^{+/+}$/*Gpr183*$^{-/-}$ bone marrow chimeras and the differentiation of *Gpr183*$^{+/+}$ and *Gpr183*$^{-/-}$ bone marrow cells into macrophages *in vitro*. Fig. S5 shows marker genes to define nonhematopoietic lung cells in IM-DTR mice by single-cell RNA sequencing (relevant to Fig. 8, F–H) as well as expression of *Ccl2* and *Csf1* in SPAM deleter mice after alveolar macrophage depletion (relevant to Fig. 8, A–D). Table S1 (related to Fig. 10) contains information on the human BAL donors that were used for single-cell RNA sequencing. Table S2 (related to all figures) provides information on reagents, assays, biological samples, mouse strains, deposited data, and software used in the study. Table S3 (related to Fig. 3, D–G; Fig. 8 A–D; Fig. S2, C–E; and Fig. S5, B and C) presents a list of antibodies used for CITE-seq analysis of SPAM deleter mice.

Data availability

Single-cell RNA-sequencing data (read counts) from bronchiectasis patients are available at GEO (accession number GSE217516). The raw sequencing data cannot be shared publicly to protect the identity of the human tissue donors as required by Swedish legislation and the European General Data Protection Regulation. The single-cell RNA-sequencing data from healthy BAL donors by Mould et al. (2021) that were used for data integration with the bronchiectasis dataset are available at GEO (accession number GSE151928). Single-cell RNA-sequencing data from lung cells of SPAM deleter mice and lung niche cells from IM-DTR mice are available at ArrayExpress (accession number E-MTAB-16590) and GEO (accession number GSE303395), respectively. All other data are available in the article itself and its supplementary materials and are also available upon reasonable request from the corresponding authors.

Acknowledgments

We would like to thank the Bioinformatics and Expression Analysis core facility, which is supported by the board of research at the Karolinska Institutet. We acknowledge Jason Cyster (University of California San Francisco, San Francisco, CA, USA) and João Pereira (Yale University, New Haven, CT, USA) for providing *Gpr183*$^{GFP/+}$ reporter mice. We thank Klas Blomgren, Ahmed Osman, and Alejandro Lastra Romero (Karolinska Institutet, Solna, Sweden) as well as Kees-Jan Pronk and Isabel Hidalgo (Lund University, Lund, Sweden) for providing bones from *Ccr2*$^{RFP/RFP}$ reporter mice and *Rag1*$^{-/-}$ mice, respectively.

This work was supported by grants from the Swedish Research Council (2019-01099 and 2022-01310), the Swedish Heart-Lung Foundation (20190198, 20220361, and 20240579), the Region Stockholm/Center for Innovative Medicine (20190152), and Karolinska Institutet (2-1060/2018, 2020-01438, 2021-00327, 2024-02407, and 2-977/2025) to T. Willinger In addition, the work was supported by a grant from Fonds Wetenschappelijk Onderzoek (G063123N) to Bart N. Lambrecht and by grants from the Fund for Scientific Research-FNRS (PDR-INTER T.0200.25), the FRFS-WELBIO (WELBIO-CR-2022A-10), the European Research Council (ERC CoG 2023 MoMac-TrajectALI: 101124390), the FEDER, and the Baillet Latour Fund to T. Marichal, as well as by grants from the Swedish Heart-Lung Foundation (2020619, 20210434, and 20220478) to A. Bossios and the European Research Council (948692) to N.K. Björkström A. Reboldi is a Burroughs-Wellcome Investigator in the Pathogenesis of Infectious Disease and is supported by National Institutes of Health grant AI155727. Open Access funding provided by Karolinska Institutet.

Author contributions: Laura Bub: formal analysis, investigation, validation, visualization, and writing—original draft. Elza Evren: formal analysis, investigation, visualization, and writing—review and editing. Stijn Verwaerde: data curation, formal analysis, investigation, methodology, visualization, and writing—review and editing. Cecilia Ruscitti: investigation, visualization, and writing—review and editing. Domien Vanneste: formal analysis, investigation, methodology, software, visualization, and writing—review and editing. Pia Ghosh: resources. Yu Gao: investigation. Natalie Sleiers: investigation. Rong Deng: investigation. Marta López Montes: investigation and writing—review and editing. Kelsey Howley: investigation. Raphaël La Rocca: formal analysis and visualization. Annika Niehrs: investigation and writing—review and editing. Vassilis Glaros: investigation. Maria Reina-Campos: formal analysis and investigation. Barbro Dahlen: funding acquisition, resources, and supervision. Anna Smed-Sörensen: resources and writing—review and editing. Harald Lund: formal analysis and investigation. Taras Kreslavsky: supervision and writing—review and editing. Niklas K. Björkström: writing—review and editing. Andrea Reboldi: investigation, methodology, and resources. Apostolos Bossios: funding acquisition, project administration, resources, supervision, and writing—review and editing. Thomas Marichal: conceptualization, formal analysis, funding acquisition, methodology, project administration, resources, supervision, validation, visualization, and writing—review and editing. Bart N. Lambrecht: conceptualization, formal analysis, funding acquisition, methodology, project administration, resources, supervision, and writing—review and editing. Tim

Willinger: conceptualization, formal analysis, funding acquisition, methodology, project administration, resources, supervision, visualization, and writing—original draft, review, and editing.

Disclosures: A. Bossios reported grants from AstraZeneca, other from AstraZeneca, other from GSK, other from Sanofi, and other from Chiesi outside the submitted work. No other disclosures were reported.

Submitted: 23 December 2025
Revised: 4 February 2026
Accepted: 4 February 2026

References

Aegerter, H., J. Kulikauskaite, S. Crotta, H. Patel, G. Kelly, E.M. Hessel, M. Mack, S. Beinke, and A. Wack. 2020. Influenza-induced monocyte-derived alveolar macrophages confer prolonged antibacterial protection. *Nat. Immunol.* 21:145–157. https://doi.org/10.1038/s41590-019-0568-x

Aegerter, H., B.N. Lambrecht, and C.V. Jakubzick. 2022. Biology of lung macrophages in health and disease. *Immunity*. 55:1564–1580. https://doi.org/10.1016/j.immuni.2022.08.010

Amit, I., D.R. Winter, and S. Jung. 2016. The role of the local environment and epigenetics in shaping macrophage identity and their effect on tissue homeostasis. *Nat. Immunol.* 17:18–25. https://doi.org/10.1038/ni.3325

Arguello, R.J., A.J. Combes, R. Char, J.P. Gigan, A.I. Baaziz, E. Bousiquot, V. Camosseto, B. Samad, J. Tsui, P. Yan, et al. 2020. SCENITH: A flow cytometry-based method to functionally profile energy metabolism with single-cell resolution. *Cell Metab.* 32:1063–1075.e7. https://doi.org/10.1016/j.cmet.2020.11.007

Bain, C.C., and A.S. MacDonald. 2022. The impact of the lung environment on macrophage development, activation and function: Diversity in the face of adversity. *Mucosal Immunol.* 15:223–234. https://doi.org/10.1038/s41385-021-00480-w

Bankhead, P., M.B. Loughrey, J.A. Fernández, Y. Dombrowski, D.G. McArt, P.D. Dunne, S. McQuaid, R.T. Gray, L.J. Murray, H.G. Coleman, et al. 2017. QuPath: Open source software for digital pathology image analysis. *Sci. Rep.* 7:16878. https://doi.org/10.1038/s41598-017-17204-5

Baptista, A.P., A. Gola, Y. Huang, P. Milanez-Almeida, P. Torabi-Parizi, J.F. Urban Jr., V.S. Shapiro, M.Y. Gerner, and R.N. Germain. 2019. The chemoattractant receptor Ebi2 drives intranodal naive CD4$^+$ T cell peripheralization to promote effective adaptive immunity. *Immunity*. 50: 1188–1201.e6. https://doi.org/10.1016/j.immuni.2019.04.001

Bartlett, S., A.T. Gemiarto, M.D. Ngo, H. Sajiir, S. Hailu, R. Sinha, C.X. Foo, L. Kleynhans, H. Tshivhula, T. Webber, et al. 2020. GPR183 regulates interferons, autophagy, and bacterial growth during *Mycobacterium tuberculosis* infection and is associated with TB disease severity. *Front. Immunol.* 11:601534. https://doi.org/10.3389/fimmu.2020.601534

Bleriot, C., S. Chakarov, and F. Ginhoux. 2020. Determinants of resident tissue macrophage identity and function. *Immunity*. 52:957–970. https://doi.org/10.1016/j.immuni.2020.05.014

Bohrer, A.C., E. Castro, C.E. Tocheny, M. Assmann, B. Schwarz, E. Bohrnsen, M.A. Makiya, F. Legrand, K.L. Hilligan, P.J. Baker, et al. 2022. Rapid GPR183-mediated recruitment of eosinophils to the lung after Mycobacterium tuberculosis infection. *Cell Rep.* 40:111144. https://doi.org/10.1016/j.celrep.2022.111144

Bonnardel, J., W. T'Jonck, D. Gaublomme, R. Browaeys, C.L. Scott, L. Martens, B. Vanneste, S. De Prijck, S.A. Nedospasov, A. Kremer, et al. 2019. Stellate cells, hepatocytes, and endothelial cells imprint the kupffer cell identity on monocytes colonizing the liver macrophage niche. *Immunity*. 51:638–654.e9. https://doi.org/10.1016/j.immuni.2019.08.017

Byrne, A.J., J.E. Powell, B.J. O'Sullivan, P.P. Ogger, A. Hoffland, J. Cook, K.L. Bonner, R.J. Hewitt, S. Wolf, P. Ghai, et al. 2020. Dynamics of human monocytes and airway macrophages during healthy aging and after transplant. *J. Exp. Med.* 217:e20191236. https://doi.org/10.1084/jem.20191236

Ceglia, S., A. Berthelette, K. Howley, Y. Li, B. Mortzfeld, S.K. Bhattarai, N.K.H. Yiew, Y. Xu, R. Brink, J.G. Cyster, et al. 2023. An epithelial cell-derived metabolite tunes immunoglobulin A secretion by gut-resident plasma cells. *Nat. Immunol.* 24:531–544. https://doi.org/10.1038/s41590-022-01413-w

Chakarov, S., H.Y. Lim, L. Tan, S.Y. Lim, P. See, J. Lum, X.M. Zhang, S. Foo, S. Nakamizo, K. Duan, et al. 2019. Two distinct interstitial macrophage populations coexist across tissues in specific subtissular niches. *Science*. 363:eaau0964. https://doi.org/10.1126/science.aau0964

Chalmers, J.D., A.B. Chang, S.H. Chotirmall, R. Dhar, and P.J. McShane. 2018. Bronchiectasis. *Nat. Rev. Dis. Primers*. 4:45. https://doi.org/10.1038/s41572-018-0042-3

Cyster, J.G., E.V. Dang, A. Reboldi, and T. Yi. 2014. 25-Hydroxycholesterols in innate and adaptive immunity. *Nat. Rev. Immunol.* 14:731–743. https://doi.org/10.1038/nri3755

Daemen, S., M.M. Chan, and J.D. Schilling. 2021. Comprehensive analysis of liver macrophage composition by flow cytometry and immunofluorescence in murine NASH. *STAR Protoc.* 2:100511. https://doi.org/10.1016/j.xpro.2021.100511

Dang, E.V., and A. Reboldi. 2024. Cholesterol sensing and metabolic adaptation in tissue immunity. *Trends Immunol.* 45:861–870. https://doi.org/10.1016/j.it.2024.09.013

Dick, S.A., A. Wong, H. Hamidzada, S. Nejat, R. Nechanitzky, S. Vohra, B. Mueller, R. Zaman, C. Kantores, L. Aronoff, et al. 2022. Three tissue resident macrophage subsets coexist across organs with conserved origins and life cycles. *Sci. Immunol.* 7:eabf7777. https://doi.org/10.1126/sciimmunol.abf7777

Emgård, J., H. Kammoun, B. Garcia-Cassani, J. Chesne, S.M. Parigi, J.M. Jacob, H.W. Cheng, E. Evren, S. Das, P. Czarnewski, et al. 2018. Oxysterol sensing through the receptor GPR183 promotes the lymphoid-tissue-inducing function of innate lymphoid cells and colonic inflammation. *Immunity*. 48:120–132.e8. https://doi.org/10.1016/j.immuni.2017.11.020

Evren, E., E. Ringqvist, J.-M. Doisne, A. Thaller, N. Sleiers, R.A. Flavell, J.P. Di Santo, and T. Willinger. 2022. CD116+ fetal precursors migrate to the perinatal lung and give rise to human alveolar macrophages. *J. Exp. Med.* 219:e20210987. https://doi.org/10.1084/jem.20210987

Evren, E., E. Ringqvist, K.P. Tripathi, N. Sleiers, I.C. Rives, A. Alisjahbana, Y. Gao, D. Sarhan, T. Halle, C. Sorini, et al. 2021. Distinct developmental pathways from blood monocytes generate human lung macrophage diversity. *Immunity*. 54:259–275.e7. https://doi.org/10.1016/j.immuni.2020.12.003

Evren, E., E. Ringqvist, and T. Willinger. 2020. Origin and ontogeny of lung macrophages: From mice to humans. *Immunology*. 160:126–138. https://doi.org/10.1111/imm.13154

Foo, C.X., S. Bartlett, K.Y. Chew, M.D. Ngo, H. Bielefeldt-Ohmann, B.J. Arachchige, B. Matthews, S. Reed, R. Wang, C. Smith, et al. 2023. GPR183 antagonism reduces macrophage infiltration in influenza and SARS-CoV-2 infection. *Eur. Respir. J.* 61:2201306. https://doi.org/10.1183/13993003.01306-2022

Frascoli, M., E. Ferraj, B. Miu, J. Malin, N.A. Spidale, J. Cowan, S.C. Shissler, R. Brink, Y. Xu, J.G. Cyster, et al. 2023. Skin γδ T cell inflammatory responses are hardwired in the thymus by oxysterol sensing via GPR183 and calibrated by dietary cholesterol. *Immunity*. 56:562–575.e6. https://doi.org/10.1016/j.immuni.2023.01.025

Gatto, D., D. Paus, A. Basten, C.R. Mackay, and R. Brink. 2009. Guidance of B cells by the orphan G protein-coupled receptor EBI2 shapes humoral immune responses. *Immunity*. 31:259–269. https://doi.org/10.1016/j.immuni.2009.06.016

Gatto, D., K. Wood, I. Caminschi, D. Murphy-Durland, P. Schofield, D. Christ, G. Karupiah, and R. Brink. 2013. The chemotactic receptor EBI2 regulates the homeostasis, localization and immunological function of splenic dendritic cells. *Nat. Immunol.* 14:446–453. https://doi.org/10.1038/ni.2555

Gibbings, S.L., R. Goyal, A.N. Desch, S.M. Leach, M. Prabagar, S.M. Atif, D.L. Bratton, W. Janssen, and C.V. Jakubzick. 2015. Transcriptome analysis highlights the conserved difference between embryonic and postnatal-derived alveolar macrophages. *Blood*. 126:1357–1366. https://doi.org/10.1182/blood-2015-01-624809

Gibbings, S.L., S.M. Thomas, S.M. Atif, A.L. McCubbrey, A.N. Desch, T. Danhorn, S.M. Leach, D.L. Bratton, P.M. Henson, W.J. Janssen, and C.V. Jakubzick. 2017. Three unique interstitial macrophages in the murine lung at steady state. *Am. J. Respir. Cell Mol. Biol.* 57:66–76. https://doi.org/10.1165/rcmb.2016-0361OC

Gschwend, J., S.P.M. Sherman, F. Ridder, X. Feng, H.E. Liang, R.M. Locksley, B. Becher, and C. Schneider. 2021. Alveolar macrophages rely on GM-CSF from alveolar epithelial type 2 cells before and after birth. *J. Exp. Med.* 218:e20210745. https://doi.org/10.1084/jem.20210745

Guilliams, M., I. De Kleer, S. Henri, S. Post, L. Vanhoutte, S. De Prijck, K. Deswarte, B. Malissen, H. Hammad, and B.N. Lambrecht. 2013. Alveolar macrophages develop from fetal monocytes that differentiate into long-lived cells in the first week of life via GM-CSF. *J. Exp. Med.* 210:1977–1992. https://doi.org/10.1084/jem.20131199

Guilliams, M., A. Mildner, and S. Yona. 2018. Developmental and functional heterogeneity of monocytes. *Immunity*. 49:595–613. https://doi.org/10.1016/j.immuni.2018.10.005

Guilliams, M., and F.R. Svedberg. 2021. Does tissue imprinting restrict macrophage plasticity? *Nat. Immunol.* 22:118–127. https://doi.org/10.1038/s41590-020-00849-2

Guilliams, M., G.R. Thierry, J. Bonnardel, and M. Bajenoff. 2020. Establishment and maintenance of the macrophage niche. *Immunity*. 52:434–451. https://doi.org/10.1016/j.immuni.2020.02.015

Hashimoto, D., A. Chow, C. Noizat, P. Teo, M.B. Beasley, M. Leboeuf, C.D. Becker, P. See, J. Price, D. Lucas, et al. 2013. Tissue-resident macrophages self-maintain locally throughout adult life with minimal contribution from circulating monocytes. *Immunity*. 38:792–804. https://doi.org/10.1016/j.immuni.2013.04.004

Howley, K., A. Berthelette, S. Ceglia, J. Kang, and A. Reboldi. 2023. Embryonic type 3 innate lymphoid cells sense maternal dietary cholesterol to control local Peyer's patch development. *bioRxiv*. https://doi.org/10.1101/2023.03.19.533339 (Posted March 23, 2023).

Iliakis, C.S., S. Crotta, and A. Wack. 2025. The interplay between innate immunity and nonimmune cells in lung damage, inflammation, and repair. *Annu. Rev. Immunol.* 43:395–422. https://doi.org/10.1146/annurev-immunol-082323-031852

Jenkins, S.J., and J.E. Allen. 2021. The expanding world of tissue-resident macrophages. *Eur. J. Immunol.* 51:1882–1896. https://doi.org/10.1002/eji.202048881

Jia, J., T.M. Conlon, R.S. Sarker, D. Tasdemir, N.F. Smirnova, B. Srivastava, S.E. Verleden, G. Gunes, X. Wu, C. Prehn, et al. 2018. Cholesterol metabolism promotes B-cell positioning during immune pathogenesis of chronic obstructive pulmonary disease. *EMBO Mol. Med.* 10:e8349. https://doi.org/10.15252/emmm.201708349

Joshi, N., S. Watanabe, R. Verma, R.P. Jablonski, C.I. Chen, P. Cheresh, N.S. Markov, P.A. Reyfman, A.C. McQuattie-Pimentel, L. Sichizya, et al. 2020. A spatially restricted fibrotic niche in pulmonary fibrosis is sustained by M-CSF/M-CSFR signalling in monocyte-derived alveolar macrophages. *Eur. Respir. J.* 55:1900646. https://doi.org/10.1183/13993003.00646

Kong, W.T., M. Bied, and F. Ginhoux. 2024. Spectral flow cytometry analysis of resident tissue macrophages. *Methods Mol. Biol.* 2713:269–280. https://doi.org/10.1007/978-1-0716-3437-0_18

Kulikauskaite, J., and A. Wack. 2020. Teaching old dogs new tricks? The plasticity of lung alveolar macrophage subsets. *Trends Immunol.* 41:864–877. https://doi.org/10.1016/j.it.2020.08.008

Li, F., F. Piattini, L. Pohlmeier, Q. Feng, H. Rehrauer, and M. Kopf. 2022a. Monocyte-derived alveolar macrophages autonomously determine severe outcome of respiratory viral infection. *Sci. Immunol.* 7:eabj5761. https://doi.org/10.1126/sciimmunol.abj5761

Li, J., E. Lu, T. Yi, and J.G. Cyster. 2016. EBI2 augments Tfh cell fate by promoting interaction with IL-2-quenching dendritic cells. *Nature*. 533:110–114. https://doi.org/10.1038/nature17947

Li, X., F.W. Kolling, D. Aridgides, D. Mellinger, A. Ashare, and C.V. Jakubzick. 2022b. ScRNA-seq expression of IFI27 and APOC2 identifies four alveolar macrophage superclusters in healthy BALF. *Life Sci. Alliance*. 5:e202201458. https://doi.org/10.26508/lsa.202201458

Li, X., A.B. Mara, S.C. Musial, F.W. Kolling, S.L. Gibbings, N. Gerebtsov, and C.V. Jakubzick. 2024. Coordinated chemokine expression defines macrophage subsets across tissues. *Nat. Immunol.* 25:1110–1122. https://doi.org/10.1038/s41590-024-01826-9

Luecken, M.D., and F.J. Theis. 2019. Current best practices in single-cell RNA-seq analysis: A tutorial. *Mol. Syst. Biol.* 15:e8746. https://doi.org/10.15252/msb.20188746

Luo, M., W. Lai, Z. He, and L. Wu. 2021. Development of an optimized culture system for generating mouse alveolar macrophage-like cells. *J. Immunol.* 207:1683–1693. https://doi.org/10.4049/jimmunol.2100185

Machiels, B., M. Dourcy, X. Xiao, J. Javaux, C. Mesnil, C. Sabatel, D. Desmecht, F. Lallemand, P. Martinive, H. Hammad, et al. 2017. A gammaherpesvirus provides protection against allergic asthma by inducing the replacement of resident alveolar macrophages with regulatory monocytes. *Nat. Immunol.* 18:1310–1320. https://doi.org/10.1038/ni.3857

Madenspacher, J.H., E.D. Morrell, J.G. McDonald, B.M. Thompson, Y. Li, K.G. Birukov, A.A. Birukova, R.D. Stapleton, A. Alejo, P.W. Karmaus, et al. 2023. 25-Hydroxycholesterol exacerbates vascular leak during acute lung injury. *JCI Insight*. 8:e155448. https://doi.org/10.1172/jci.insight.155448

McCowan, J., F. Fercoq, P.M. Kirkwood, W. T'Jonck, L.M. Hegarty, C.M. Mawer, R. Cunningham, A.S. Mirchandani, A. Hoy, D.C. Humphries, et al. 2021. The transcription factor EGR2 is indispensable for tissue-specific imprinting of alveolar macrophages in health and tissue repair. *Sci. Immunol.* 6:eabj2132. https://doi.org/10.1126/sciimmunol.abj2132

Mirchandani, A.S., S.J. Jenkins, C.C. Bain, M.A. Sanchez-Garcia, H. Lawson, P. Coelho, F. Murphy, D.M. Griffith, A. Zhang, T. Morrison, et al. 2022. Hypoxia shapes the immune landscape in lung injury and promotes the persistence of inflammation. *Nat. Immunol.* 23:927–939. https://doi.org/10.1038/s41590-022-01216-z

Misharin, A.V., L. Morales-Nebreda, P.A. Reyfman, C.M. Cuda, J.M. Walter, A.C. McQuattie-Pimentel, C.I. Chen, K.R. Anekalla, N. Joshi, K.J.N. Williams, et al. 2017. Monocyte-derived alveolar macrophages drive lung fibrosis and persist in the lung over the life span. *J. Exp. Med.* 214:2387–2404. https://doi.org/10.1084/jem.20162152

Mould, K.J., C.M. Moore, S.A. McManus, A.L. McCubbrey, J.D. McClendon, C.L. Griesmer, P.M. Henson, and W.J. Janssen. 2021. Airspace macrophages and monocytes exist in transcriptionally distinct subsets in healthy adults. *Am. J. Respir. Crit. Care Med.* 203:946–956. https://doi.org/10.1164/rccm.202005-1989OC

Neehus, A.-L., B. Carey, M. Landekic, P. Panikulam, G. Deutsch, M. Ogishi, C.A. Arango-Franco, Q. Philippot, M. Modaresi, I. Mohammadzadeh, et al. 2024. Human inherited CCR2 deficiency underlies progressive polycystic lung disease. *Cell*. 187:390–408.e3. https://doi.org/10.1016/j.cell.2024.05.021

Neupane, A.S., M. Willson, A.K. Chojnacki, E.S.C.F. Vargas, C. Morehouse, A. Carestia, A.E. Keller, M. Peiseler, A. DiGiandomenico, M.M. Kelly, et al. 2020. Patrolling alveolar macrophages conceal Bacteria from the immune system to maintain homeostasis. *Cell*. 183:110–125.e11. https://doi.org/10.1016/j.cell.2020.08.020

Ngo, M.D., S. Bartlett, H. Bielefeldt-Ohmann, C.X. Foo, R. Sinha, B.J. Arachchige, S. Reed, T. Mandrup-Poulsen, M.M. Rosenkilde, and K. Ronacher. 2022. A blunted GPR183/oxysterol Axis during dysglycemia results in delayed recruitment of macrophages to the lung during Mycobacterium tuberculosis infection. *J. Infect. Dis.* 225:2219–2228. https://doi.org/10.1093/infdis/jiac102

Peng, W., D. Vanneste, D. Bejarano, J. Abinet, M. Meunier, C. Radermecker, F. Perin, D. Cataldo, F. Bureau, A. Schlitzer, et al. 2025. Endothelial-driven TGFβ signaling supports lung interstitial macrophage development from monocytes. *Sci. Immunol.* 10:eadr4977. https://doi.org/10.1126/sciimmunol.adr4977

Pereira, J.P., L.M. Kelly, Y. Xu, and J.G. Cyster. 2009. EBI2 mediates B cell segregation between the outer and centre follicle. *Nature*. 460:1122–1126. https://doi.org/10.1038/nature08226

Rauschmeier, R., C. Gustafsson, A. Reinhardt, N. A-Gonzalez, L. Tortola, D. Cansever, S. Subramanian, R. Taneja, M.J. Rossner, M.H. Sieweke, et al. 2019. Bhlhe40 and Bhlhe41 transcription factors regulate alveolar macrophage self-renewal and identity. *EMBO J.* 38:e101233. https://doi.org/10.15252/embj.2018101233

Ray, A., and B.N. Dittel. 2010. Isolation of mouse peritoneal cavity cells. *J. Vis. Exp.* 28:1488. https://doi.org/10.3791/1488

Rodero, M.P., L. Poupel, P.L. Loyher, P. Hamon, F. Licata, C. Pessel, D.A. Hume, C. Combadiere, and A. Boissonnas. 2015. Immune surveillance of the lung by migrating tissue monocytes. *Elife*. 4:e07847. https://doi.org/10.7554/eLife.07847

Ruscitti, C., J. Abinet, P. Marechal, M. Meunier, C. de Meeus, D. Vanneste, P. Janssen, M. Dourcy, M. Thiry, F. Bureau, et al. 2024. Recruited atypical Ly6G(+) macrophages license alveolar regeneration after lung injury. *Sci. Immunol.* 9:eado1227. https://doi.org/10.1126/sciimmunol.ado1227

Sabatel, C., C. Radermecker, L. Fievez, G. Paulissen, S. Chakarov, C. Fernandes, S. Olivier, M. Toussaint, D. Pirottin, X. Xiao, et al. 2017. Exposure to bacterial CpG DNA protects from airway allergic inflammation by expanding regulatory lung interstitial macrophages. *Immunity*. 46:457–473. https://doi.org/10.1016/j.immuni.2017.02.016

Schlitzer, A., N. McGovern, P. Teo, T. Zelante, K. Atarashi, D. Low, A.W. Ho, P. See, A. Shin, P.S. Wasan, et al. 2013. IRF4 transcription factor-dependent CD11b+ dendritic cells in human and mouse control mucosal IL-17 cytokine responses. *Immunity*. 38:970–983. https://doi.org/10.1016/j.immuni.2013.04.011

Schmidt, U., M. Weigert, C. Broaddus, G. Myers. 2018. Cell Detection with Star-convex Polygons. *arXiv*. https://doi.org/10.48550/arXiv.1806.03535 (Preprint posted November 8, 2018)

Schneider, C., S.P. Nobs, M. Kurrer, H. Rehrauer, C. Thiele, and M. Kopf. 2014. Induction of the nuclear receptor PPAR-γ by the cytokine GM-CSF is critical for the differentiation of fetal monocytes into alveolar macrophages. *Nat. Immunol.* 15:1026–1037. https://doi.org/10.1038/ni.3005

Schyns, J., Q. Bai, C. Ruscitti, C. Radermecker, S. De Schepper, S. Chakarov, F. Farnir, D. Pirottin, F. Ginhoux, G. Boeckxstaens, et al. 2019. Nonclassical tissue monocytes and two functionally distinct populations of interstitial macrophages populate the mouse lung. *Nat. Commun.* 10: 3964. https://doi.org/10.1038/s41467-019-11843-0

Serbina, N.V., and E.G. Pamer. 2006. Monocyte emigration from bone marrow during bacterial infection requires signals mediated by chemokine receptor CCR2. *Nat. Immunol.* 7:311–317. https://doi.org/10.1038/ni1309

Shibata, Y., P.Y. Berclaz, Z.C. Chroneos, M. Yoshida, J.A. Whitsett, and B.C. Trapnell. 2001. GM-CSF regulates alveolar macrophage differentiation and innate immunity in the lung through PU.1. *Immunity*. 15:557–567. https://doi.org/10.1016/s1074-7613(01)00218-7

Soucie, E.L., Z. Weng, L. Geirsdottir, K. Molawi, J. Maurizio, R. Fenouil, N. Mossadegh-Keller, G. Gimenez, L. VanHille, M. Beniazza, et al. 2016. Lineage-specific enhancers activate self-renewal genes in macrophages and embryonic stem cells. *Science*. 351:aad5510. https://doi.org/10.1126/science.aad5510

Street, K., D. Risso, R.B. Fletcher, D. Das, J. Ngai, N. Yosef, E. Purdom, and S. Dudoit. 2018. Slingshot: Cell lineage and pseudotime inference for single-cell transcriptomics. *BMC Genomics*. 19:477. https://doi.org/10.1186/s12864-018-4772-0

Subramanian, S., C.J. Busch, K. Molawi, L. Geirsdottir, J. Maurizio, S. Vargas Aguilar, H. Belahbib, G. Gimenez, R.A.A. Yuda, M. Burkon, et al. 2022. Long-term culture-expanded alveolar macrophages restore their full epigenetic identity after transfer in vivo. *Nat. Immunol.* 23:458–468. https://doi.org/10.1038/s41590-022-01146-w

Szabo, P.A., P. Dogra, J.I. Gray, S.B. Wells, T.J. Connors, S.P. Weisberg, I. Krupska, R. Matsumoto, M.M.L. Poon, E. Idzikowski, et al. 2021. Longitudinal profiling of respiratory and systemic immune responses reveals myeloid cell-driven lung inflammation in severe COVID-19. *Immunity*. 54:797–814.e6. https://doi.org/10.1016/j.immuni.2021.03.005

T'Jonck, W., and C.C. Bain. 2023. The role of monocyte-derived macrophages in the lung: It's all about context. *Int. J. Biochem. Cell Biol.* 159:106421. https://doi.org/10.1016/j.biocel.2023.106421

Theobald, H., D.A. Bejarano, N. Katzmarski, J. Haub, J. Schulte-Schrepping, J. Yu, K. Bassler, A.L. Ament, C. Osei-Sarpong, F. Piattini, et al. 2024. Apolipoprotein E controls Dectin-1-dependent development of monocyte-derived alveolar macrophages upon pulmonary β-glucan-induced inflammatory adaptation. *Nat. Immunol.* 25:994–1006. https://doi.org/10.1038/s41590-024-01830-z

Trzebanski, S., J.S. Kim, N. Larossi, A. Raanan, D. Kancheva, J. Bastos, M. Haddad, A. Solomon, E. Sivan, D. Aizik, et al. 2024. Classical monocyte ontogeny dictates their functions and fates as tissue macrophages. *Immunity*. 57:1225–1242.e6. https://doi.org/10.1016/j.immuni.2024.06.011

Ural, B.B., S.T. Yeung, P. Damani-Yokota, J.C. Devlin, M. de Vries, P. Vera-Licona, T. Samji, C.M. Sawai, G. Jang, O.A. Perez, et al. 2020. Identification of a nerve-associated, lung-resident interstitial macrophage subset with distinct localization and immunoregulatory properties. *Sci. Immunol.* 5:eaax8756. https://doi.org/10.1126/sciimmunol.aax8756

van de Laar, L., W. Saelens, S. De Prijck, L. Martens, C.L. Scott, G. Van Isterdael, E. Hoffmann, R. Beyaert, Y. Saeys, B.N. Lambrecht, and M. Guilliams. 2016. Yolk sac macrophages, fetal liver, and adult monocytes can colonize an empty niche and develop into functional tissue-resident macrophages. *Immunity*. 44:755–768. https://doi.org/10.1016/j.immuni.2016.02.017

Vanneste, D., Q. Bai, S. Hasan, W. Peng, D. Pirottin, J. Schyns, P. Marechal, C. Ruscitti, M. Meunier, Z. Liu, et al. 2023. MafB-restricted local monocyte proliferation precedes lung interstitial macrophage differentiation. *Nat. Immunol.* 24:827–840. https://doi.org/10.1038/s41590-023-01468-3

Verwaerde, S., J.F. Hastir, S.T.T. Schetters, U. Smole, L. Seys, A.P. Baptista, K. English, M.J. Schuijs, H. Aegerter, K.F.A. Van Damme, et al. 2025. Innate type 2 lymphocytes trigger an inflammatory switch in alveolar macrophages. *Immunity*. 59:60–78.e9. https://doi.org/10.1016/j.immuni.2025.11.015

Wculek, S.K., I. Heras-Murillo, A. Mastrangelo, D. Mananes, M. Galan, V. Miguel, A. Curtabbi, C. Barbas, N.S. Chandel, J.A. Enriquez, et al. 2023. Oxidative phosphorylation selectively orchestrates tissue macrophage homeostasis. *Immunity*. 56:516–530 e519. https://doi.org/10.1016/j.immuni.2023.01.011

Wendisch, D., O. Dietrich, T. Mari, S. von Stillfried, I.L. Ibarra, M. Mittermaier, C. Mache, R.L. Chua, R. Knoll, S. Timm, et al. 2021. SARS-CoV-2 infection triggers profibrotic macrophage responses and lung fibrosis. *Cell*. 184:6243–6261.e27. https://doi.org/10.1016/j.cell.2021.11.033

Yi, T., and J.G. Cyster. 2013. EBI2-mediated bridging channel positioning supports splenic dendritic cell homeostasis and particulate antigen capture. *Elife*. 2:e00757. https://doi.org/10.7554/eLife.00757

Yi, T., X. Wang, L.M. Kelly, J. An, Y. Xu, A.W. Sailer, J.A. Gustafsson, D.W. Russell, and J.G. Cyster. 2012. Oxysterol gradient generation by lymphoid stromal cells guides activated B cell movement during humoral responses. *Immunity*. 37:535–548. https://doi.org/10.1016/j.immuni.2012.06.015

Yona, S., K.W. Kim, Y. Wolf, A. Mildner, D. Varol, M. Breker, D. Strauss-Ayali, S. Viukov, M. Guilliams, A. Misharin, et al. 2013. Fate mapping reveals origins and dynamics of monocytes and tissue macrophages under homeostasis. *Immunity*. 38:79–91. https://doi.org/10.1016/j.immuni.2012.12.001

Yu, X., A. Buttgereit, I. Lelios, S.G. Utz, D. Cansever, B. Becher, and M. Greter. 2017. The cytokine TGF-β promotes the development and homeostasis of alveolar macrophages. *Immunity*. 47:903–912.e4. https://doi.org/10.1016/j.immuni.2017.10.007

Zhou, X., R.A. Franklin, M. Adler, T.S. Carter, E. Condiff, T.S. Adams, S.D. Pope, N.H. Philip, M.L. Meizlish, N. Kaminski, and R. Medzhitov. 2022. Microenvironmental sensing by fibroblasts controls macrophage population size. *Proc. Natl. Acad. Sci. USA*. 119:e2205360119. https://doi.org/10.1073/pnas.2205360119

Zhou, X., R.A. Franklin, M. Adler, J.B. Jacox, W. Bailis, J.A. Shyer, R.A. Flavell, A. Mayo, U. Alon, and R. Medzhitov. 2018. Circuit design features of a stable two-cell system. *Cell*. 172:744–757.e17. https://doi.org/10.1016/j.cell.2018.01.015

Supplemental material

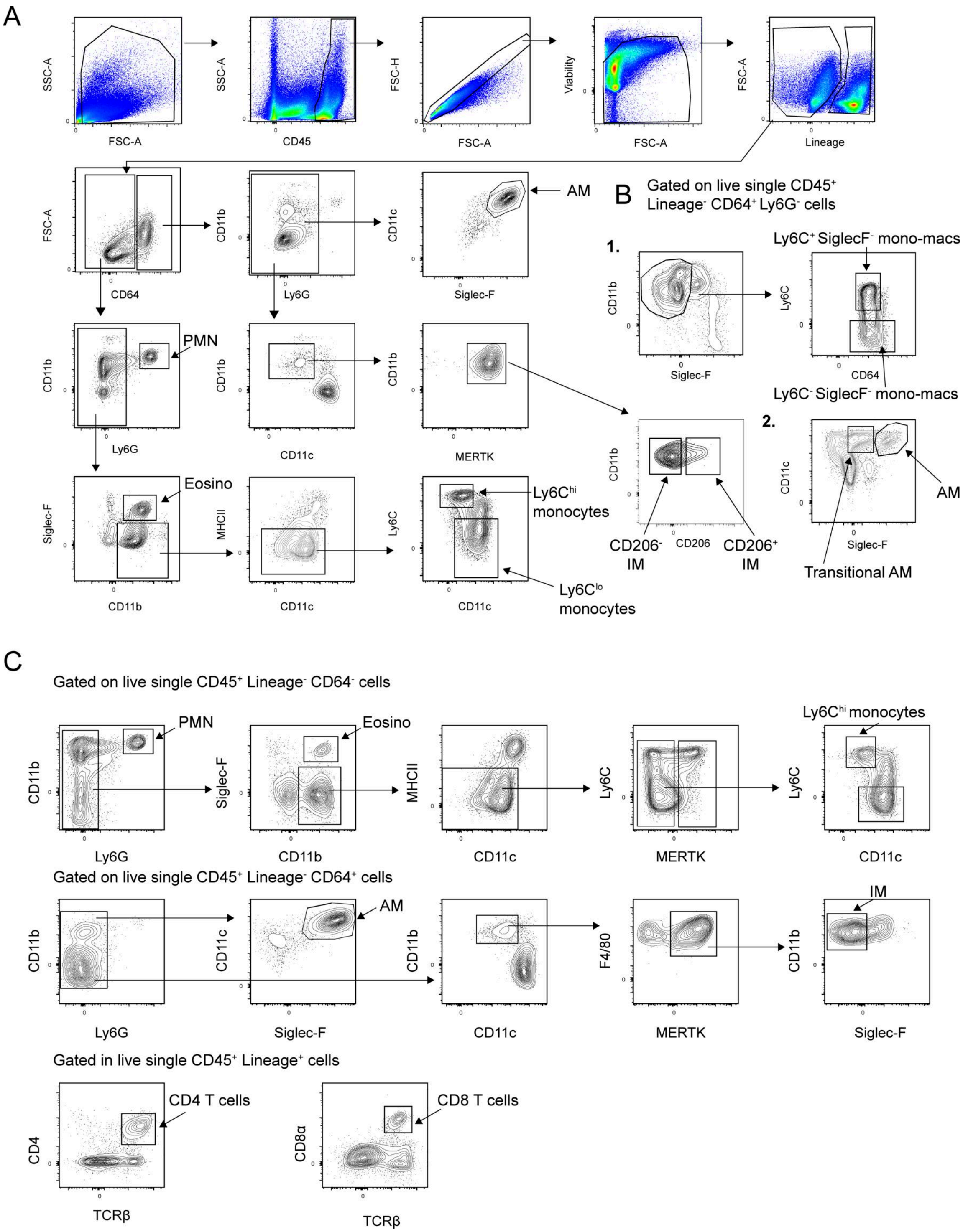

Figure S1. **Gating strategy for immune cells in the mouse lung. (A)** Gating strategy to identify lung myeloid cells in *Gpr183*$^{GFP/+}$ reporter mice (see Fig. 1 A and Fig. 2, A and B). Lung cells were first gated on live single CD45$^+$ lineage (CD3/CD19/NK1.1)$^-$ cells before separating myeloid cells into the indicated CD64$^+$ macrophage and CD64$^-$ cell populations as shown. Alveolar macrophages in BAL fluid (Fig. 2, A and F) were gated as CD64$^+$Ly6G$^-$CD11c$^+$SiglecF$^+$ cells as shown here for alveolar macrophages in the lung. AMs, alveolar macrophages; Eosino, eosinophils; FSC-A, forward scatter area; FSC-H, forward scatter height; FSC-W, forward scatter width; IMs, interstitial macrophages; PMNs, polymorphonuclear neutrophils; SSC-A, side scatter area. Data are representative of at least three independent experiments with a total of *n* = 5–6 mice. **(B)** Gating strategy to identify lung macrophage populations in chimeras 3 wk after bone marrow reconstitution (see Fig. 2 E and Fig. 7 A). Cells were pre-gated as live single CD45$^+$lineage$^-$CD64$^+$Ly6G$^-$ cells as in panel A and then separated into the different macrophage populations. Mono-mac, monocyte-macrophages. Data are representative of at least two independent experiments with a total of *n* = 4–13 mice. **(C)** Gating strategy to identify lung immune cells in the steady-state lung of *Gpr183*$^{+/+}$ and *Gpr183*$^{-/-}$ mice (Fig. 2 C) and in the lung of bone marrow chimeras (Fig. 4, A–D; Fig. 6, B and D; and Fig. 7 C). After pre-gating on live single CD45$^+$lineage$^-$CD64$^-$, CD45$^+$lineage$^-$CD64$^+$, or CD45$^+$lineage$^-$ cells as in panel A, the indicated cell populations were gated as shown. Data are representative of at least two independent experiments with a total of *n* = 4–19 mice.

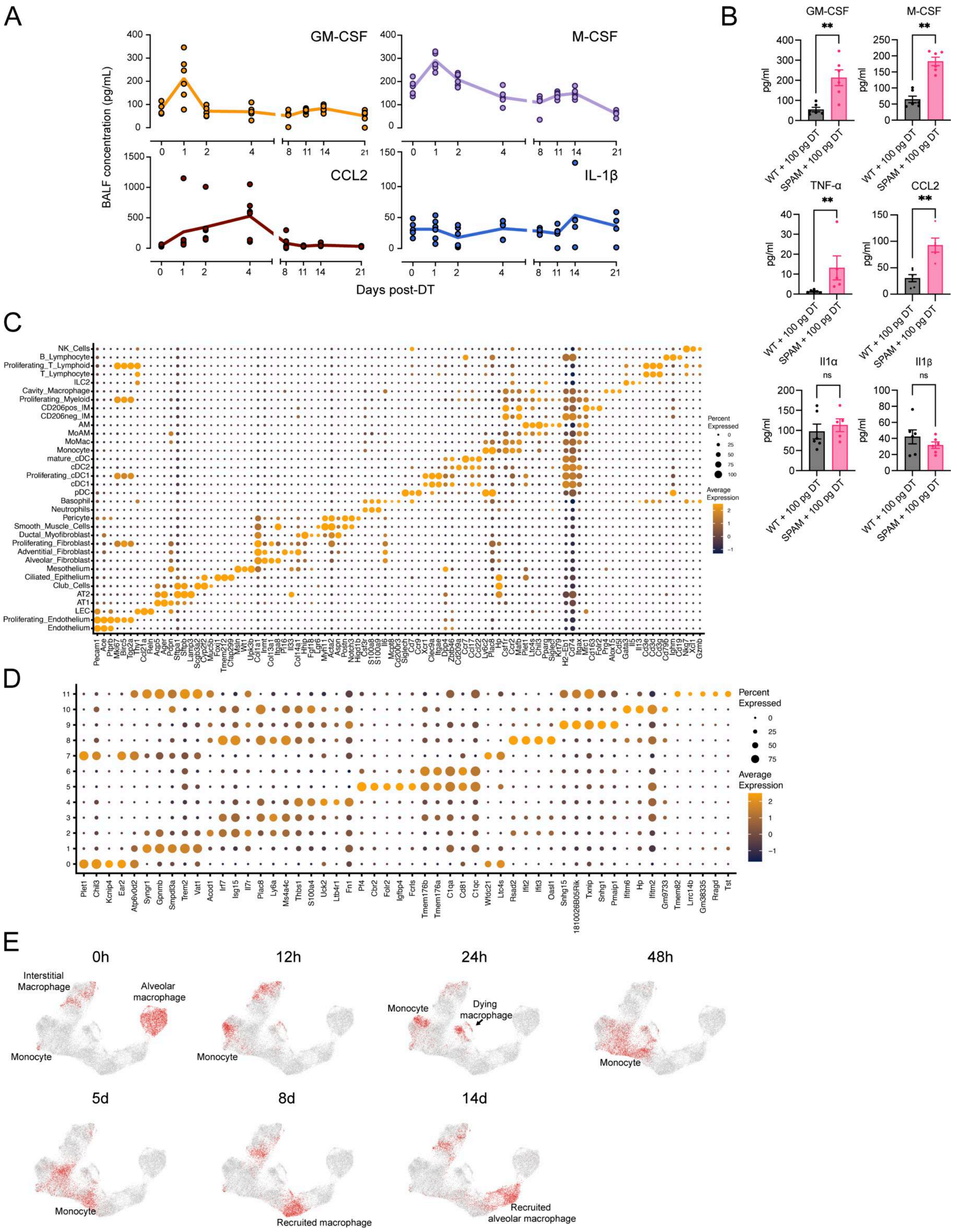

Figure S2. **Experimental depletion of alveolar macrophages in SPAM deleter mice. (A)** Concentrations of GM-CSF, M-CSF, CCL2, and IL-1β protein in the BAL fluid (BALF) of SPAM deleter mice at the indicated time points after intratracheal administration of 100 ng DT. Data are from a single experiment with *n* = 4–6 mice per time point. **(B)** Concentrations of the indicated cytokines and chemokines in the BALF of WT (*Epx*$^{\mathrm{Cre}}$ *Siglecf*$^{+/+}$) and SPAM deleter (*Epx*$^{\mathrm{Cre}}$ *Siglecf*$^{\mathrm{Lox\text{-}DTR\text{-}Lox}}$) mice 24 h after DT administration. Data are from a single experiment with *n* = 6 mice per time point. Data are represented as mean ± SEM. **P < 0.01 by two-tailed Mann–Whitney test. **(C)** Dot plot showing expression of curated marker genes to annotate the lung cell clusters in Fig. 3 E and Fig. 8 A from SPAM deleter mice as determined by single-cell RNA sequencing. **(D)** Dot plot showing expression of the top five differentially expressed genes for the lung monocyte-macrophage clusters in Fig. 3 F from SPAM deleter mice as determined by single-cell RNA sequencing. **(E)** Repopulation of alveolar macrophages after experimental depletion in SPAM deleter mice as shown by single-cell RNA sequencing. Red dots overlaid on the UMAP from Fig. 3 F show cells present in the lung of SPAM deleter mice at the indicated time points before and after alveolar macrophage depletion with DT. Data in panels C–E are from one single-cell RNA-sequencing experiment with *n* = 4 mice per time point.

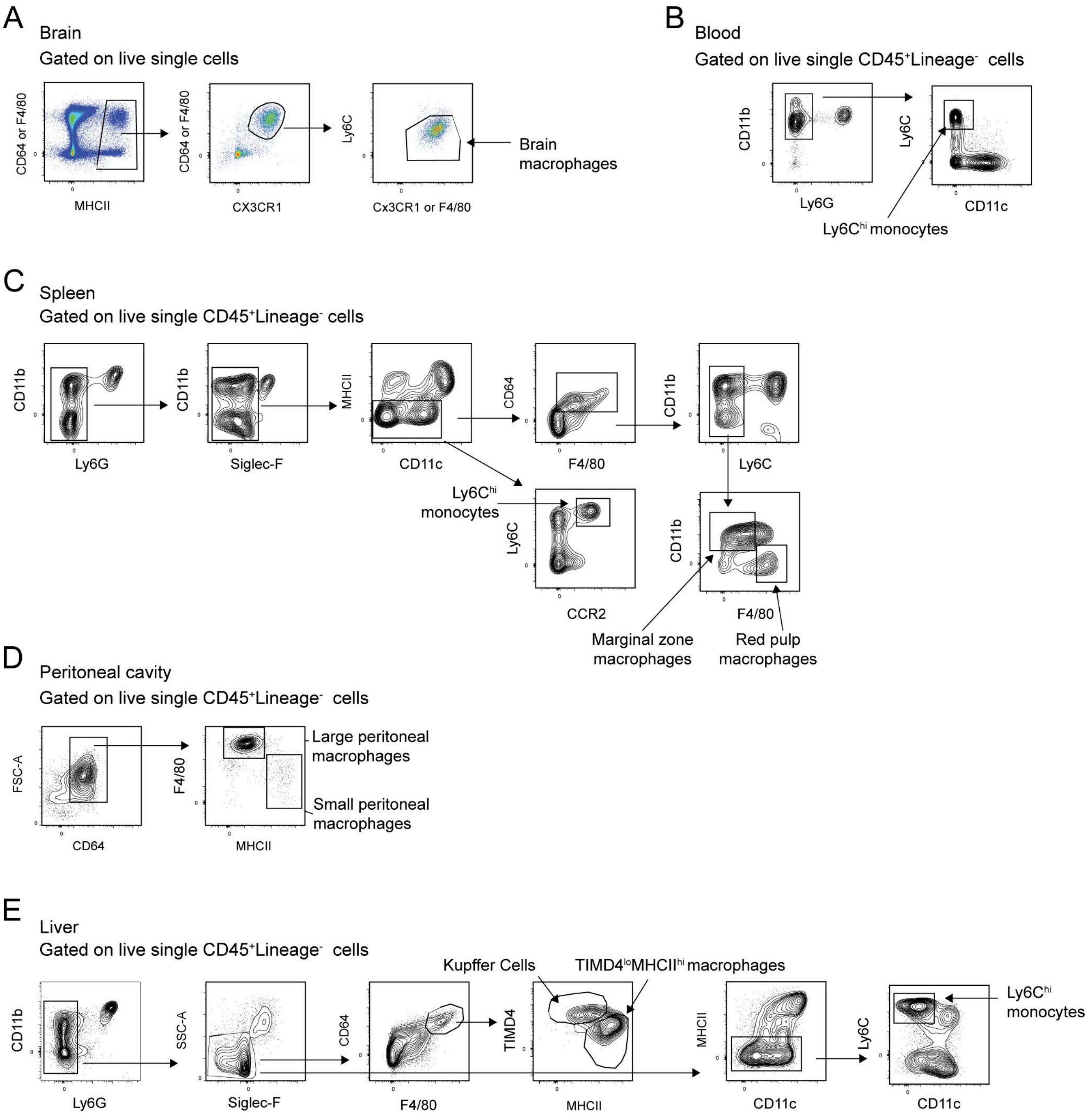

Figure S3. **Gating strategy for monocytes and macrophages in tissues other than lung. (A–E)** Gating strategies to identify the indicated monocyte and macrophage populations in Fig. 4 E in (A) brain, (B) blood, (C) spleen, (D) peritoneal cavity, and (E) liver. Data are representative of one (peritoneal cavity), three (brain), four (liver), or five (spleen) independent bone marrow chimera experiments with a total of *n* = 6–32 mice per tissue.

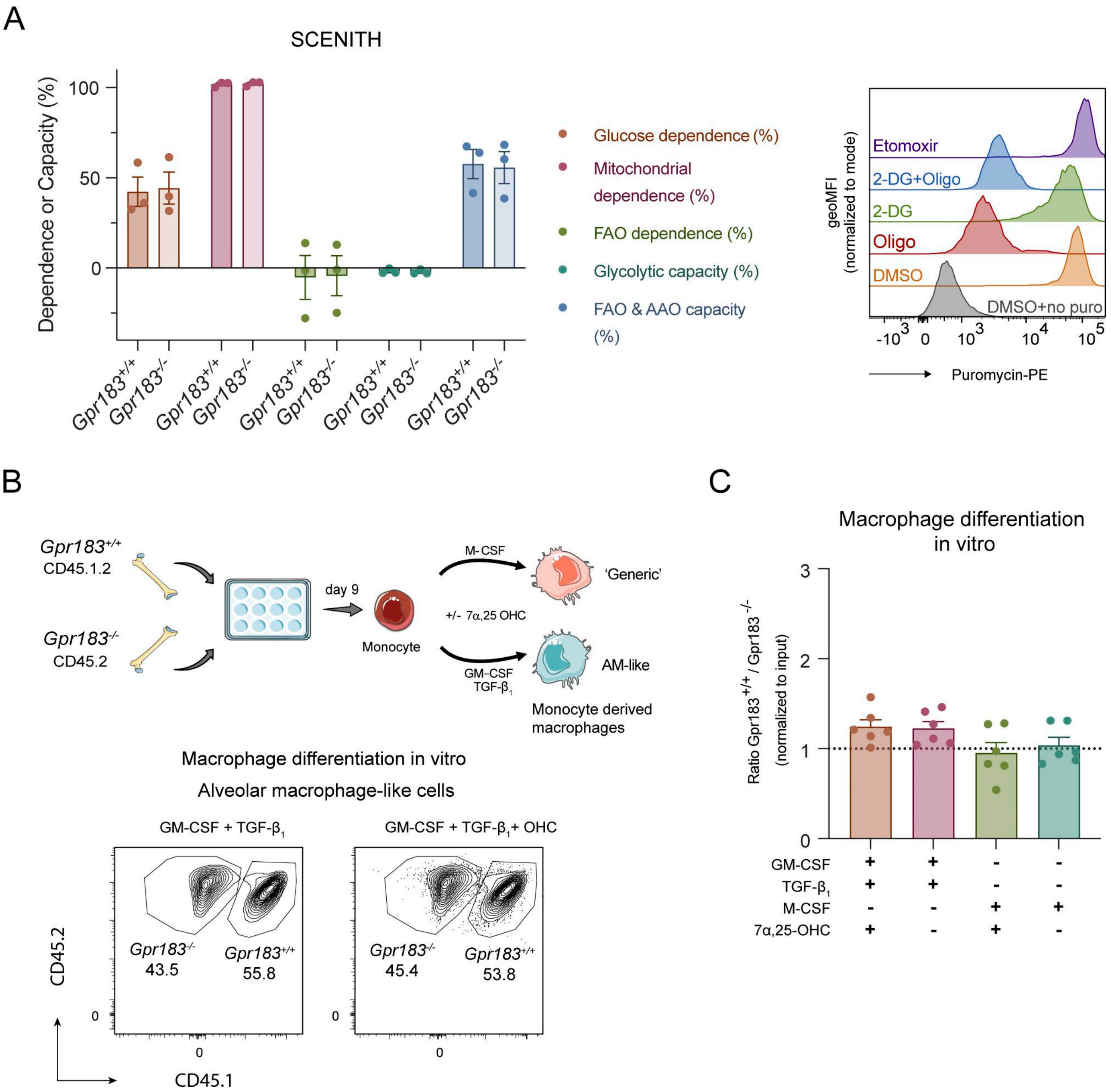

Figure S4. **GPR183 is dispensable for macrophage differentiation *in vitro* and for acquisition of homeostatic alveolar macrophage metabolism.** **(A)** Metabolism of alveolar macrophages isolated from competitive *Gpr183*$^{+/+}$/*Gpr183*$^{-/-}$ bone marrow chimeras 9–11 wk after bone marrow transfer. Metabolic dependencies and capacities were determined by SCENITH (Arguello et al., 2020) as described in the Materials and methods. AAO, amino acid oxidation; 2-DG, 2-deoxy-D-glucose; FAO, fatty acid oxidation; Oligo, oligomycin; Puro, puromycin. Data are represented as mean ± SEM. Data are combined from two independent experiments. For each experiment, BAL cells from two to three chimeric mice were pooled. In one of the two independent experiments, a sufficient number of cells allowed for two technical replicates. **(B and C)** *In vitro* differentiation of *Gpr183*$^{+/+}$ and *Gpr183*$^{-/-}$ macrophages. Bone marrow cells from *Gpr183*$^{+/+}$ and *Gpr183*$^{-/-}$ mice were mixed 1:1 and cultured with the indicated cytokines to generate macrophages in the absence or presence of 7α,25-dihydroxycholesterol (7α,25-OHC). The ratio of *Gpr183*$^{+/+}$/*Gpr183*$^{-/-}$ macrophages was normalized to the bone marrow input of each independent experiment. Data are represented as mean ± SEM. Data are pooled from three independent experiments with a total of n = 3 mice per genotype and two technical replicates per experiment. Panel B was adapted from Servier Medical Art.

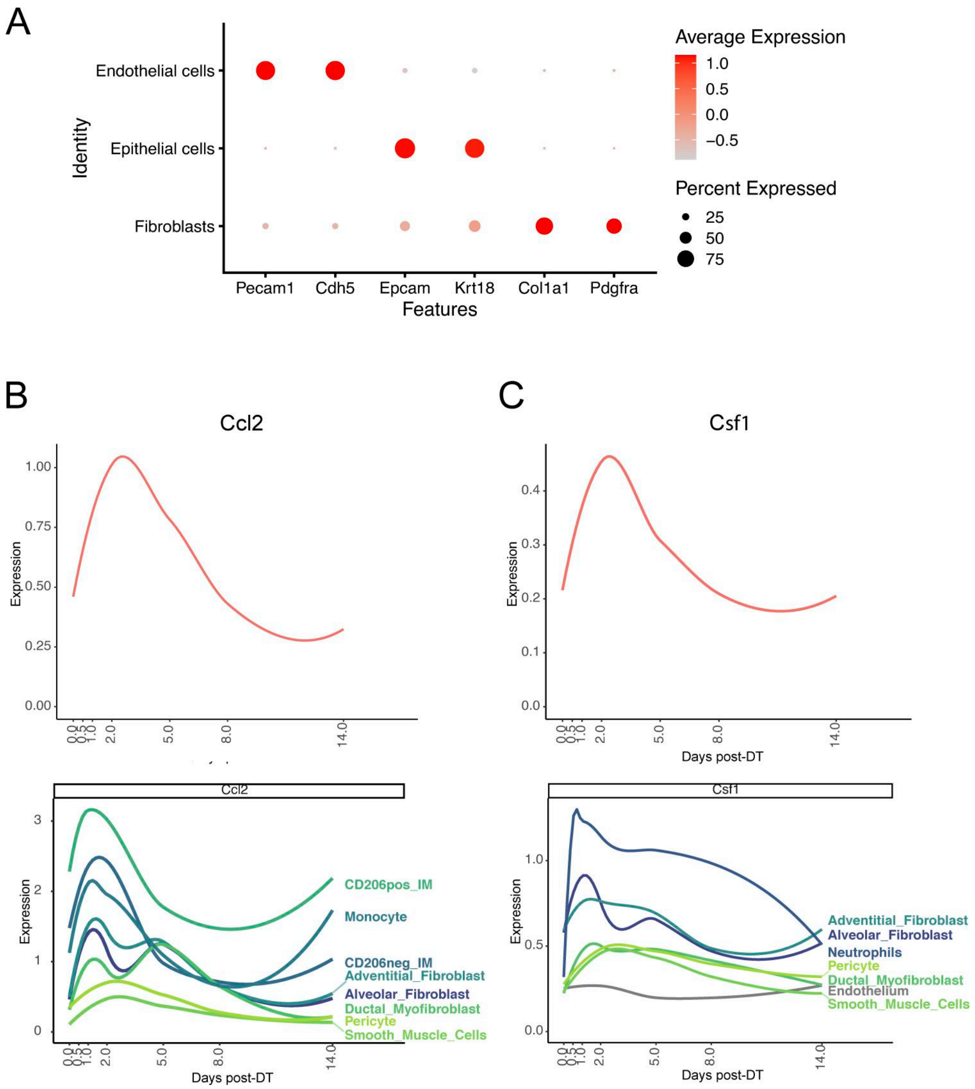

Figure S5. **Expression of *Ccl2* and *Csf1* in SPAM deleter mice after alveolar macrophage depletion. (A)** Dot plot showing expression of marker genes to define endothelial cells, epithelial cells, and fibroblasts in the lung of IM-DTR mice as in Fig. 8, F–G. Data are from one single-cell RNA-sequencing experiment with *n* = 3–4 mice per time point. **(B and C)** Time course of *Ccl2* (A) and *Csf1* (B) expression in the lung clusters of SPAM deleter mice from Fig. 3 E. Data are from one single-cell RNA-sequencing experiment with *n* = 4 mice per time point. IM, interstitial macrophage.

Provided online are Table S1, Table S2, and Table S3. Table S1 shows the information on human BAL donors used for single-cell RNA sequencing. Table S2 shows the key resources used in the study. Table S3 shows the antibodies for CITE-seq SPAM deleter mice